

## Article

# Intelligent Backstepping Control of Permanent Magnet-Assisted Synchronous Reluctance Motor Position Servo Drive with Recurrent Wavelet Fuzzy Neural Network

Faa-Jeng Lin <sup>1,\*</sup> , Ming-Shi Huang <sup>2</sup>, Yu-Chen Chien <sup>1</sup>  and Shih-Gang Chen <sup>2</sup>

<sup>1</sup> Department of Electrical Engineering, National Central University, Taoyuan 32001, Taiwan; 110521077@cc.ncu.edu.tw

<sup>2</sup> Department of Electrical Engineering, National Taipei University of Technology, Taipei 10608, Taiwan; simonh@ntut.edu.tw (M.-S.H.); csg12388@gmail.com (S.-G.C.)

\* Correspondence: linfj@ee.ncu.edu.tw; Tel.: +886-3-422-7151 (ext. 34532)

**Abstract:** An intelligent servo drive system for a permanent magnet-assisted synchronous reluctance motor (PMASynRM) that can adapt to the control requirements considering the motor's nonlinear and time-varying natures is developed in this study. A recurrent wavelet fuzzy neural network (RWFNN) with intelligent backstepping control is proposed to achieve this. In this study, first, a maximum torque per ampere (MTPA) controlled PMASynRM servo drive is introduced. A lookup table (LUT) is created, which is based on finite element analysis (FEA) results by using ANSYS Maxwell-2D dynamic model to determine the current angle command of the MTPA. Next, a backstepping control (BSC) system is created to accurately follow the desired position in the PMASynRM servo drive system while maintaining robust control characteristics. However, designing an efficient BSC for practical applications becomes challenging due to the lack of prior uncertainty information. To overcome this challenge, this study introduces an RWFNN as an approximation for the BSC, aiming to alleviate the limitations of the traditional BSC approach. An enhanced adaptive compensator is also incorporated into the RWFNN to handle potential approximation errors effectively. In addition, to ensure the stability of the RWFNN, the Lyapunov stability method is employed to develop online learning algorithms for the RWFNN and to guarantee its asymptotic stability. The proposed intelligent backstepping control with recurrent wavelet fuzzy neural network (IBSCRWFNN) demonstrates remarkable effectiveness and robustness in controlling the PMASynRM servo drive, as evidenced by the experimental results.

**Keywords:** permanent magnet-assisted synchronous reluctance motor (PMASynRM); maximum torque per ampere (MTPA); finite element analysis (FEA); backstepping control (BSC); recurrent wavelet fuzzy neural network (RWFNN); intelligent backstepping control recurrent wavelet fuzzy neural network (IBSCRWFNN)



**Citation:** Lin, F.-J.; Huang, M.-S.; Chien, Y.-C.; Chen, S.-G. Intelligent Backstepping Control of Permanent Magnet-Assisted Synchronous Reluctance Motor Position Servo Drive with Recurrent Wavelet Fuzzy Neural Network. *Energies* **2023**, *16*, 5389. <https://doi.org/10.3390/en16145389>

Academic Editors: Loránd Szabó and Feng Chai

Received: 14 June 2023

Revised: 10 July 2023

Accepted: 13 July 2023

Published: 14 July 2023



**Copyright:** © 2023 by the authors. Licensee MDPI, Basel, Switzerland. This article is an open access article distributed under the terms and conditions of the Creative Commons Attribution (CC BY) license (<https://creativecommons.org/licenses/by/4.0/>).

## 1. Introduction

The permanent magnet synchronous motor (PMSM) is an electric motor type that has found extensive applications in diverse fields, including electric vehicles, industrial automation, robotics, and aerospace plane [1,2]. Compared to conventional induction motors, PMSM exhibits high efficiency exceeding 90%, resulting in substantial energy savings. It also possesses a high magnetic field strength and low internal resistance, enabling PMSM to achieve a higher power density and greater output power within a relatively smaller volume. Moreover, PMSM offers excellent torque-speed performance and sensitive current control ability, making it ideal for precision applications such as automatic control systems [3–5]. Despite its advantages, rare-earth elements such as NdFeB can be costly and raise concerns regarding the supply chain monopoly and trade wars. Additionally, high-performance applications using PMSM face challenges such as operating

at the region of flux-weakening control with large direct-axis current and the potential for uncontrolled generator mode due to the flux linkages generated by permanent magnets (PM). These drawbacks limit the potential benefits of PMSM and should be taken into account when considering their use in specific applications. Hence, there is a need to decrease the utilization of rare-earth PMs.

Due to their rapid dynamic response, wide speed range, affordability, and high efficiency, the synchronous reluctance motor (SynRM) has gained significant popularity and is now utilized in numerous applications. Unlike induction motors and PMSM, SynRM offers inherent advantages by eliminating the need for permanent magnetic materials, cages, and excitation windings. This not only enhances its robustness but also reduces its overall cost, making it an attractive alternative [6–9]. However, SynRM has limited overload capability compared to other types of motors, meaning that it may not be suitable for applications that require high levels of torque for short periods of time. Based on the aforementioned reasons, a relatively new machine, known as the permanent magnet-assisted synchronous reluctance motor (PMASynRM), has been developed to address the challenges associated with the scarcity of rare-earth PMs. One approach to mitigating these difficulties involves reducing the amount of rare-earth PMs used in the rotor or replacing them with ferrite magnets [10–13]. Maximum torque per ampere (MTPA) has been widely utilized as a control strategy in PMSMs and SynRMs control to maximize output torque [14–19]. In [17,18], the MTPA control strategy has been implemented in the control of IPMSMs and SynRMs to determine the ideal current angle for maximizing the output torque based on a given stator current. Moreover, in [19], an MTPA control with nonlinear simultaneous equations was derived from the Lagrange multiplier method, which could be solved by numerical algorithms. The MTPA control technology enables the production of equivalent torque with minimal current. It achieves this by identifying the ideal current angle that maximizes output torque at a given stator current while also minimizing copper loss during the process. However, PMASynRM has inherent drawbacks, such as nonlinear and time-varying control characteristics, which make achieving high-performance servo applications and the traditional MTPA quite challenging [20].

The backstepping control (BSC), despite its advantages in providing a recursive and systematic design methodology for nonlinear feedback control, may encounter undesired chattering phenomena due to the presence of a sign function. Several approaches, such as adaptive control [21] and intelligent control [22], have been proposed for integration with BSC to overcome this issue and enhance control performance. In [21], a PMSM drive system was targeted, and an adaptive backstepping (ABS) control approach was introduced as a solution. The purpose of this method is to achieve precise tracking responses by utilizing the robustness properties of the ABS control. In [22], to overcome the limitations posed by the nonlinear and time-varying control natures of a SynRM, a robust position controller was devised for a SynRM servo drive system. This was achieved through the introduction of an intelligent BSC approach, employing a recurrent feature selection fuzzy neural network. In addition, to improve control performance and facilitate model-free controller design, intelligent control methods, including fuzzy mechanisms, NNs, and FNNs, have been widely used as universal approximators in various studies. Among these, the FNN has been particularly popular due to its combined advantages of neural networks and fuzzy logic and has been applied in various fields, such as photovoltaic systems, robotics, and motor control [23–25]. In fact, the FNN's robustness and convenience have garnered attention for controlling permanent magnet linear synchronous motors [25]. Moreover, the recurrent neural network (RNN) is capable of mapping and storing temporal information dynamically [26,27], utilizing time delays from earlier states, and approximate information can be obtained from internal feedback states. This makes RFNN a better option for dynamic performance than the pure feedforward FNN. Furthermore, the wavelet transform is an influential and effective technique used for the analysis of intricate time-varying signals. It offers numerous advantages and capabilities, making it a valuable tool in signal processing [28], and has been extensively studied for its applications that combine

the learning capabilities of artificial neural network (ANN) and wavelet decomposition. Recently, researchers have proposed integrating wavelet functions into FNNs to create the wavelet fuzzy neural network (WFNN) with the goal of improving adaptive and learning capabilities for complex engineering problems [29]. By analyzing non-stationary signals to identify local details, reducing data complexity and handling uncertainty through fuzzy logic, and leveraging NNs' self-learning characteristics to improve model accuracy, the WFNN is capable of describing nonlinear systems with uncertainties and possesses a fast learning capability. Additionally, this study proposes an intelligent control system using the capabilities of FNN, RNN, and WNN, where an online trained recurrent wavelet fuzzy neural network (RWFNN) [30] is utilized to enhance control performance.

High-performance applications of PMASynRM are limited due to nonlinear and time-varying control features. Therefore, the purpose of this article is to develop a high-performance PMASynRM servo drive that simultaneously achieves robust position control and high energy efficiency by using intelligent backstepping control recurrent wavelet fuzzy neural network (IBSCRWFNN) control with MTPA. To address the issue of MTPA, a Maxwell 2D simulation tool is employed in the design process of the PMASynRM. Then, the optimal current angle command for MTPA control is subsequently analyzed using finite element analysis (FEA), and apply the result by a lookup table (LUT) method to ensure proper functionality. Moreover, the PMASynRM servo drive is controlled by using the BSC to solve the presence of unavoidable uncertain system dynamics in the PMASynRM servo drive system. However, the bound of lumped uncertainty in the BSC is difficult to determine in real-life situations. To overcome this issue, the suggested method involves approximating the BSC using the RWFNN. Furthermore, this research incorporates an adaptive compensator to account for potential deviations resulting from the approximation of the RWFNN. In addition, the utilization of the Lyapunov stability method to generate online learning algorithms [22] for the IBSCRWFNN is proposed, ensuring robust performance in position control. The rest of this study is organized as follows: in Section 2, the focus will be on describing the modeling of the position servo drive system for PMASynRM with MTPA control based on the results of FEA. In Section 3, the PMASynRM servo drive is controlled by using the BSC to solve the presence of unavoidable uncertainties. To overcome the difficulty of the BSC, the RWFNN is discussed in Section 4. In Section 5, the Lyapunov stability method is proposed to generate online learning algorithms for the IBSCRWFNN. Section 6 will present the experimental results of the PI control, BSC, and the proposed IBSCRWFNN control. Finally, the research findings are thoroughly discussed in Section 7, presenting the conclusive remarks.

## 2. Modeling of PMASynRM Position Servo Drive System

### 2.1. Modeling of PMASynRM Servo Drive System

The stator voltage equations of PMASynRM in the  $d$ - $q$  reference frame can be formulated as follows:

$$v_d = R_s i_d + \frac{d}{dt} \lambda_d - \omega_e \lambda_q \quad (1)$$

$$v_q = R_s i_q + \frac{d}{dt} \lambda_q + \omega_e \lambda_d \quad (2)$$

where  $R_s$  is the stator resistance;  $v_d$  and  $v_q$  are the  $d$ -axis and  $q$ -axis voltage;  $i_d$  and  $i_q$  are the  $d$ -axis and  $q$ -axis stator currents;  $\lambda_d$  and  $\lambda_q$  are the  $d$ -axis and  $q$ -axis flux linkages;  $\omega_e$  is the rotor electrical angular velocity. Furthermore, the flux linkage equations in the  $d$ - $q$  reference frame are represented in the following:

$$\lambda_q = L_q i_q \quad (3)$$

$$\lambda_d = L_d i_d + \lambda_m \quad (4)$$

The equations above denote the  $d$ -axis and  $q$ -axis inductances as  $L_d$  and  $L_q$ , respectively, and  $\lambda_m$  as rotor PM flux. Neglecting magnetic saturation, the resulting electromagnetic torque in the  $d$ - $q$  reference frame of PMASynRM can be represented by the following equation:

$$T_e = \frac{3P}{2} [\lambda_m i_q + (L_d - L_q) i_d i_q] \quad (5)$$

where  $P$  is the pole number. Both PMASynRM and PMSM have electromagnetic torque consisting of reluctance torque and PM torque. However, in the case of PMASynRM, the reluctance torque plays the main driving role owing to the substantial disparity between the inductance values of the  $d$ -axis and  $q$ -axis inductances. The expression for the mechanical dynamic equation of the PMASynRM is as follows:

$$T_e = J \frac{d\omega_r}{dt} + B\omega_r + T_L \quad (6)$$

$J$  represents the inertia coefficient;  $B$  represents the damping coefficient;  $\omega_r$  is the speed response;  $T_L$  represents the external load and friction torque.

## 2.2. PMASynRM Position Servo Drive System

The PMASynRM utilized in this study is a 4-pole, 36-slot motor with a power rating of 4.5 kW, voltage rating of 214 V, current rating of 9.4 A, a rated speed of 1500 rpm, and a maximum torque of 25 Nm. The mechanical designed parameters for the PMASynRM and the specifications of the servo drive system are outlined in detail in Tables 1 and 2.

**Table 1.** Mechanical designed parameters of PMASynRM.

Parameters	Values
Pole number	4 pole
Slot number	36 slot
Air gap length	0.3 mm
Rotor inner diameter	31 mm
Rotor outer diameter	94.4 mm
Stator inner diameter	95 mm
Stator outer diameter	160 mm
Stack length	150 mm

**Table 2.** Specifications of PMASynRM servo drive.

Parameters	Values
Power rating	4.5 kW
Phase voltage rating	214 V
Phase current rating	9.4 Arms (delta)
Speed rating	1500 rpm
Torque rating	25 Nm
$d$ -axis inductance	19.6 mH
$q$ -axis inductance	84.3 mH
Stator resistance	1.01 $\Omega$
Inertia coefficient	0.0069 Nm/(rad/s <sup>2</sup> )
Damping coefficient	0.0013 Nm/(rad/s)
Magnetic flux	0.0854 Wb
DC-link	540 V
Sampling time of current/speed and position loop	0.1 ms/1 ms
Switching frequency	20 kHz
Encoder	2500 counts/turn

A typical PMASynRM position servo drive with coordinate transformation includes proportional position control, PI speed control, LUT for current angle, and PI current controllers, as illustrated in Figure 1.  $\theta_r^*$  is the position command;  $\theta_r$  is the position response;  $\theta_e$  is the rotor electrical position;  $\omega_r^*$  is the speed command. The  $d$ - $q$  axis current commands are represented by  $i_d^*$  and  $i_q^*$  respectively. The three-phase currents are denoted by  $i_a$ ,  $i_b$ , and  $i_c$ . Similarly, the  $d$ - $q$  axis voltage commands are represented by  $v_d^*$  and  $v_q^*$  respectively. By utilizing Hall current sensors with a transformation ratio of 1 V/6.67 A with an analog-to-digital converter (ADC), it is very effective to measure the three-phase currents. By implementing the space vector pulse width modulation (SVPWM) technique, control of the voltage source inverter (VSI) can be achieved. The VSI operates at a switching frequency of 20 kHz. Moreover, the VSI employs a silicon carbide (SiC) power MOSFET, which has a voltage rating of 900 V and a current rating of 36 A. Furthermore, using a load driver in torque control mode to control an industrial PMSM as the load for the PMASynRM, the performance of the position servo drive system for the PMASynRM is evaluated. In addition, a torque meter is connected to measure the torque output. The QEP interface is used to connect the encoder to the DSP, as illustrated in Figure 1.

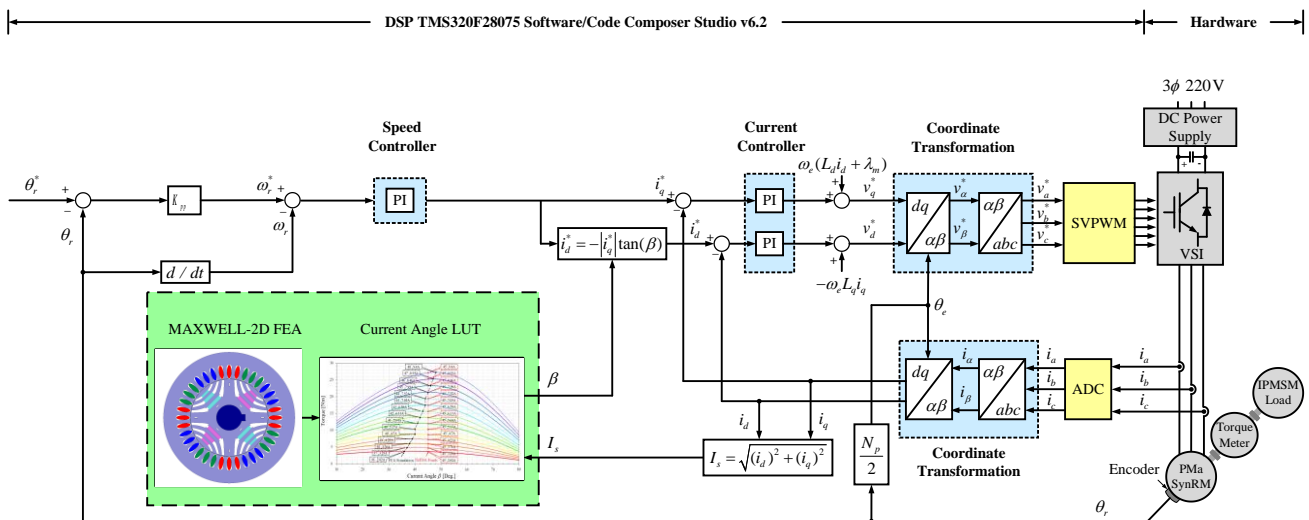


Figure 1. PI Controlled PMASynRM position servo drive.

### 2.3. Speed and Position Controllers Design

The speed and position controllers discussed in this article utilize PI controllers. These controllers are designed based on the controlled plants' small signal models. The speed controller depicted in Figure 2, where  $s$  is the Laplace operator, assumes ideal conditions where  $T_L = 0$  and sets  $i_d^* = -5A$ . By referring to Equations (7) and (8), as well as Table 2, the torque constant can be deduced as  $K_t = 1.2267$ .

$$T_e = K_t i_q^* \tag{7}$$

$$K_t = \frac{3P}{2} [\lambda_m + (L_d - L_q) i_d^*] \tag{8}$$

Moreover, the bode diagrams of the speed-controlled plant and the loop gain are shown in Figure 3. The design requirements for the speed controller include a desired bandwidth (BW)  $f = 20$  Hz and phase margin (PM)  $\phi_m = 70^\circ$ . The graphical representation in Figure 3 reveals that the controlled plant necessitates compensation of  $-3.01$  dB and  $-20.1^\circ$ . The obtained result of the PI speed controller is

$$K_P + \frac{K_I}{s} = 0.664 + \frac{30.5385}{s} \tag{9}$$

where  $K_P$  is a proportional gain;  $K_I$  is an integral gain;  $s$  is the Laplace operator. Furthermore, the position controller depicted in Figure 4 utilizes a proportional controller  $K_{PP}$ . In addition, the bode diagrams of the position-controlled plant and the loop gain are shown in Figure 5. The design requirements for the speed controller include a desired bandwidth (BW)  $f = 2$  Hz and phase margin (PM)  $\phi_m = 70^\circ$ . The graphical representation in Figure 5 reveals that the controlled plant necessitates compensation of 21.8 dB and  $-19.5^\circ$ . Since the position controller consists of a single constant term, it can only compensate for the gain through a proportional gain  $K_{PP}$  as follows:

$$K_{PP} = 12.3 \tag{10}$$

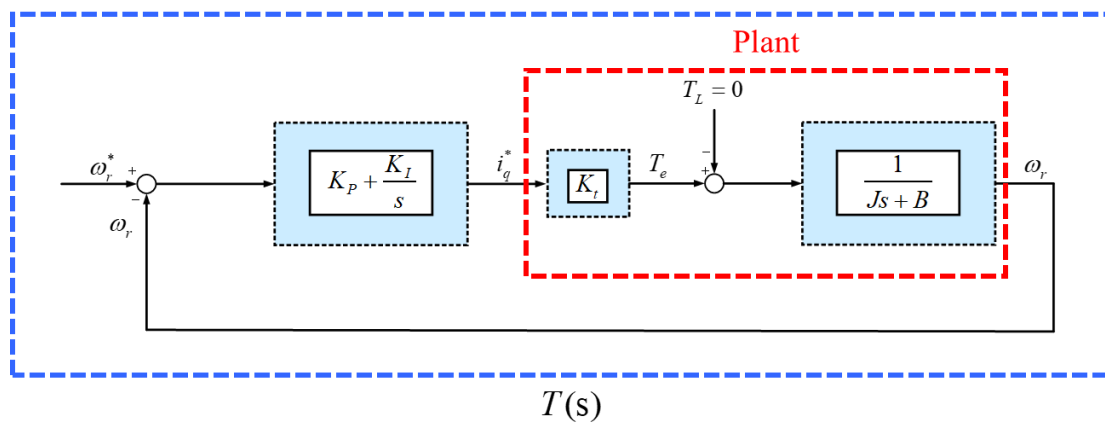


Figure 2. PI speed controller.

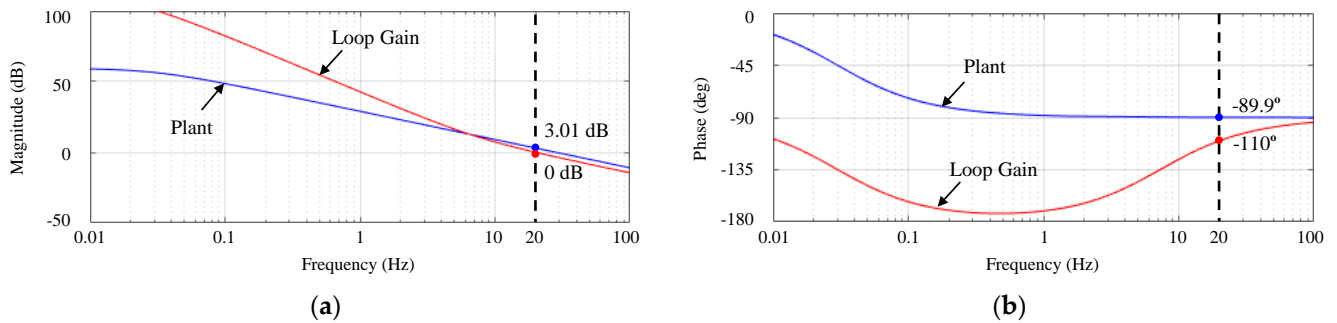


Figure 3. Bode diagrams of speed controller. (a) Magnitude; (b) Phase.

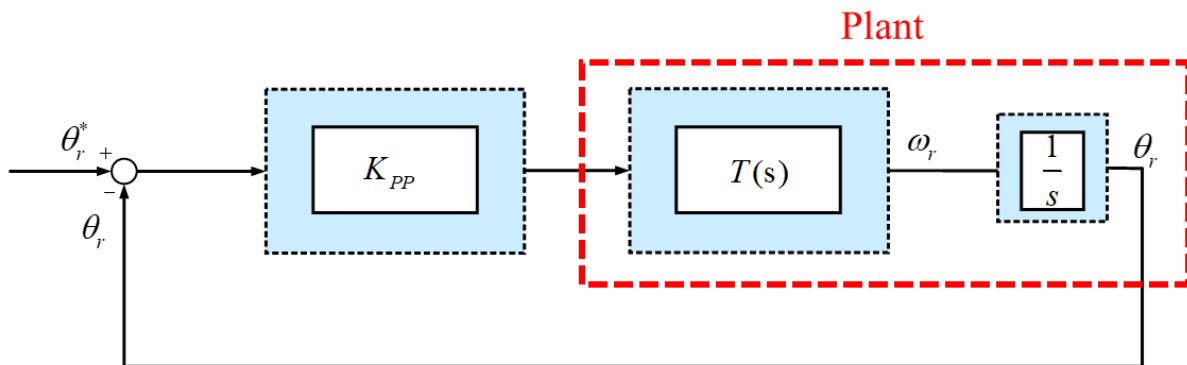


Figure 4. Proportional position controller.

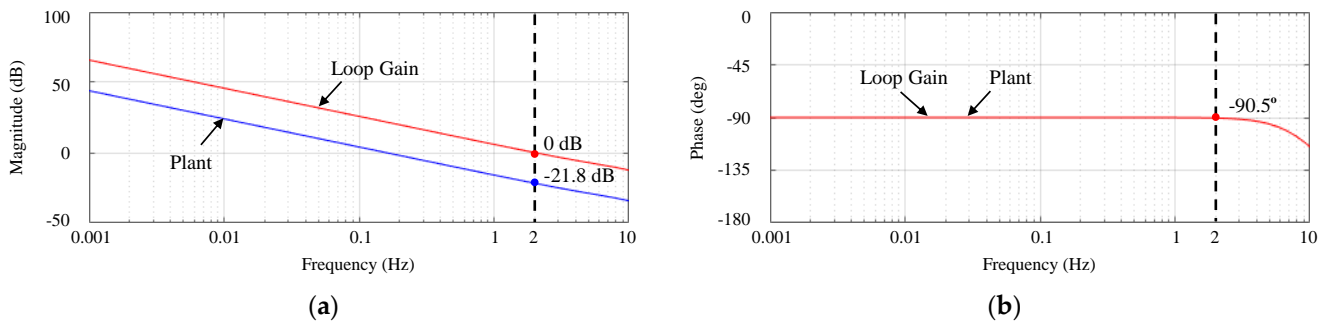


Figure 5. Bode diagrams of position controller. (a) Magnitude; (b) Phase.

### 3. BSC System

To rewrite the ideal dynamic equation using Equations (5) and (6), it can be expressed as follows:

$$\dot{\omega}_r = -\frac{\bar{B}}{\bar{J}}\omega_r + \frac{3P[\bar{\lambda}_m + (\bar{L}_d - \bar{L}_q)i_d^*]}{4\bar{J}}i_q^* - \frac{T_L}{\bar{J}} = A_m\omega_r + B_m i_q^* + C_m T_L \quad (11)$$

where  $A_m = -\frac{\bar{B}}{\bar{J}}$ ;  $B_m = \frac{3P[\bar{\lambda}_m + (\bar{L}_d - \bar{L}_q)i_d^*]}{4\bar{J}}$ ;  $C_m = -\frac{1}{\bar{J}}$ ; The symbol “-” represents the nominal value. Considering the presence of uncertainties necessitates a rewrite of the dynamic Equation (11) as follows:

$$\dot{\omega}_r = (A_m + \Delta A_m)\omega_r + (B_m + \Delta B_m)U + (C_m + \Delta C_m)T_L = A_m\omega_r + B_m U + F \quad (12)$$

where  $U = i_q^*$  is the torque current command, the time-varying parameter variations are indicated by  $\Delta A_m$ ,  $\Delta B_m$ , and  $\Delta C_m$ . Moreover,  $F$  represents the lumped uncertainty, which is defined as follows:

$$F = \Delta A_m\omega_r + \Delta B_m U + (C_m + \Delta C_m)T_L, |F| \leq F_b \quad (13)$$

and  $F_b$  is defined as lumped uncertainty bound. Furthermore, the following definitions are used for the error in position tracking and its derivative:

$$e_1 = \theta_r^*(t) - \theta_r(t) \quad (14)$$

$$\dot{e}_1 = \dot{\theta}_r^*(t) - \dot{\theta}_r(t) \quad (15)$$

The term  $\dot{\theta}_r^*(t) = \omega_r^*(t)$  can be regarded as a virtual control input, and the following stabilizing function  $\lambda_1$  is defined:

$$\lambda_1 = -c_1 e_1 - \omega_r^*(t) \quad (16)$$

The constant  $c_1$  is a positive value, and the first Lyapunov function is selected as

$$V_1 = \frac{1}{2}e_1^2 > 0 \quad (17)$$

The function  $V_1$  is positive definite. In addition, the definition of the virtual control error is as follows:

$$e_2 = \omega_r(t) + \lambda_1 = \omega_r(t) - c_1 e_1 - \omega_r^*(t) \quad (18)$$

Obtaining the derivative of  $V_1$  can be performed as follows:

$$\dot{V}_1 = e_1 \dot{e}_1 = e_1(-e_2 - c_1 e_1) = -e_1 e_2 - c_1 e_1^2 \quad (19)$$

Assuming that  $e_2 = 0$  is satisfied, then the derivative of  $V_1$  will be negative. Additionally, the derivative of  $e_2$  can be obtained as

$$\dot{e}_2 = \dot{\omega}_r(t) + \dot{\lambda}_1 = \dot{\omega}_r(t) - c_1\dot{e}_1 - \dot{\omega}_r^*(t) \quad (20)$$

The replacement of Equation (12) with Equation (20) yields the following equation:

$$\dot{e}_2 = A_m\omega_r(t) + B_mU + F - c_1\dot{e}_1 - \dot{\omega}_r^*(t) \quad (21)$$

Then, the selection of the second Lyapunov function is performed as follows:

$$V_2 = \frac{1}{2}e_1^2 + \frac{1}{2}e_2^2 = V_1 + \frac{1}{2}e_2^2 > 0 \quad (22)$$

where  $V_2$  is a positive-definite function. The derivative of  $V_2$  can be obtained by

$$\begin{aligned} \dot{V}_2 &= \dot{V}_1 + e_2\dot{e}_2 = -e_1e_2 - c_1e_1^2 + e_2\dot{e}_2 = -c_1e_1^2 + e_2(-e_1 + \dot{e}_2) \\ &= -c_1e_1^2 + e_2(A_m\dot{\theta}_r(t) + B_mU + F - c_1\dot{e}_1 - \dot{\omega}_r^*(t) - e_1) \end{aligned} \quad (23)$$

To ensure system stability based on Lyapunov's condition,  $\dot{V}_2$  must be negative semidefinite. Consequently, utilizing Equation (23), a BSC control law is proposed as follows [22]:

$$U_{BSC} = B_m^{-1}[-A_m\dot{\theta}_r(t) + c_1\dot{e}_1 + \dot{\omega}_r^*(t) + e_1 - c_2e_2 - F_b\text{sgn}(e_2)] \quad (24)$$

where  $c_2$  is a positive constant;  $\text{sgn}(\cdot)$  is a sign function. The dynamic Equation (12) of the PMASynRM position servo drive system indicates that the implementation of the BSC law, as outlined in Equation (24), ensures system stability. By substituting Equation (24) into Equation (23), we can derive the resulting equation as follows:

$$\begin{aligned} \dot{V}_2 &= -c_1e_1^2 + e_2[-c_2e_2 - F_b\text{sgn}(e_2) + F] \\ &= -c_1e_1^2 - c_2e_2^2 - |e_2|F_b + e_2F \\ &\leq -c_1e_1^2 - c_2e_2^2 - |e_2|F_b + |e_2||F| \\ &\leq -c_1e_1^2 - c_2e_2^2 - |e_2|(F_b - |F|) \\ &\leq -c_1e_1^2 - c_2e_2^2 \leq 0. \end{aligned} \quad (25)$$

Thus, parametric uncertainty and external torque disturbance do not affect the stability of the BSC system. Figure 6 illustrates the control system's capability to maintain stability even in the presence of disturbances. However, it is worth noting that the use of a sign function can lead to chattering phenomena. A boundary layer approach can be employed to mitigate this issue by substituting the sign function with a saturation function. This substitution helps reduce the occurrence of chattering phenomena.

$$\text{sat}(e_2) = \begin{cases} 1 & e_2 > \phi \\ \frac{e_2}{\phi}, & -\phi \leq e_2 \leq \phi \\ -1 & e_2 < -\phi \end{cases} \quad (26)$$

The saturation function is denoted as  $\text{sat}$ ; the boundary layer is set as  $\phi > 0$ . Thus, the BSC control law (24) is modified as follows:

$$U_{BSC} = B_m^{-1}[-A_m\dot{\theta}_r(t) + c_1\dot{e}_1 + \dot{\omega}_r^*(t) + e_1 - c_2e_2 - F_b\text{sat}(e_2)] \quad (27)$$

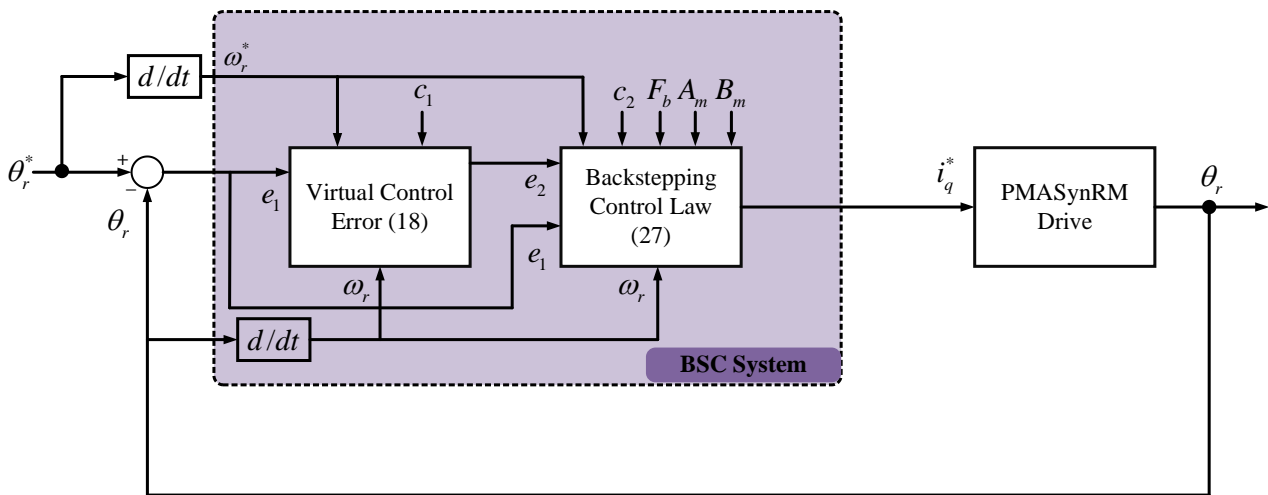


Figure 6. Control block diagram of BSC controlled PMASynRM position servo drive.

#### 4. IBSCRWFNN System

The BSC system can ensure system stability when  $|F| \leq F_b$ . However, the lumped uncertainty is unknown in the real world, making it challenging to determine the upper bound  $F_b$ . Moreover, asymptotic stability is a crucial requirement for position servo drives. In order to overcome the limitations associated with the BSC law described in Equation (27), an RWFNN controller [30] is proposed. The primary objective of designing the RWFNN controller is to achieve improved performance by providing an effective approximation of the BSC law. The control block diagram of the IBSCRWFNN system is shown in Figure 7. The control law for the IBSCRWFNN system is designed as follows to achieve asymptotic stability in position servo drives.

$$U = \hat{U}_{RWFNN} + \hat{U}_c \tag{28}$$

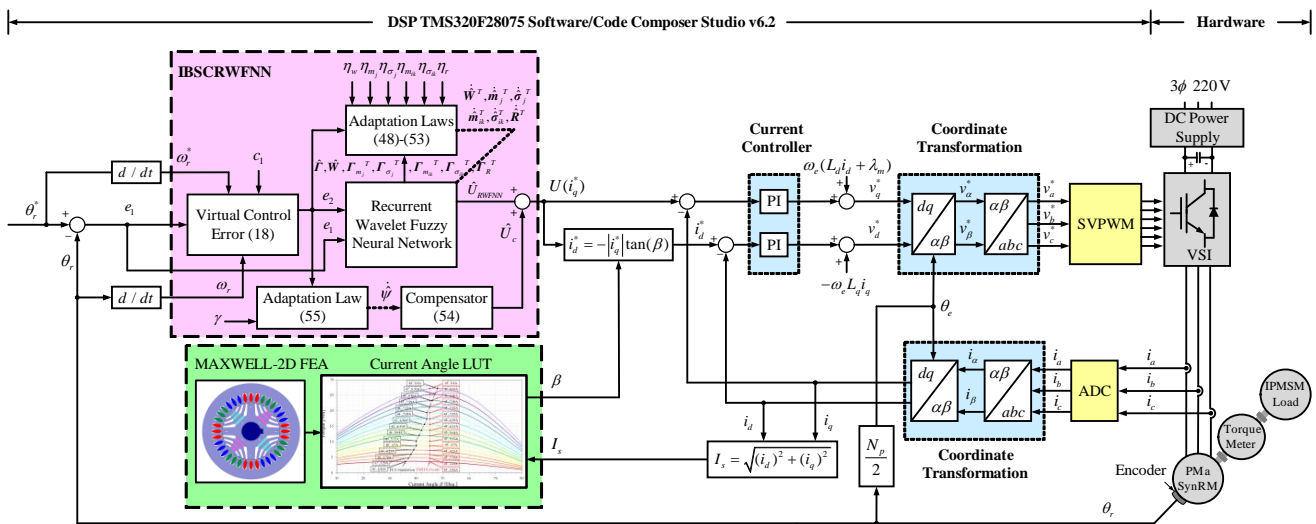


Figure 7. IBSCRWFNN controlled PMASynRM position servo drive.

The RWFNN controller, represented by  $\hat{U}_{RWFNN}$ , plays a crucial role in learning the BSC law to handle unknown system dynamics. Simultaneously, the compensator, denoted as  $\hat{U}_c$ , is specifically designed to minimize the approximated error introduced by the RWFNN controller. This combination of  $\hat{U}_{RWFNN}$  and  $\hat{U}_c$  effectively addresses the unknown system dynamics and improves the overall performance of the control system.

Furthermore, the network structure is represented in Figure 8.

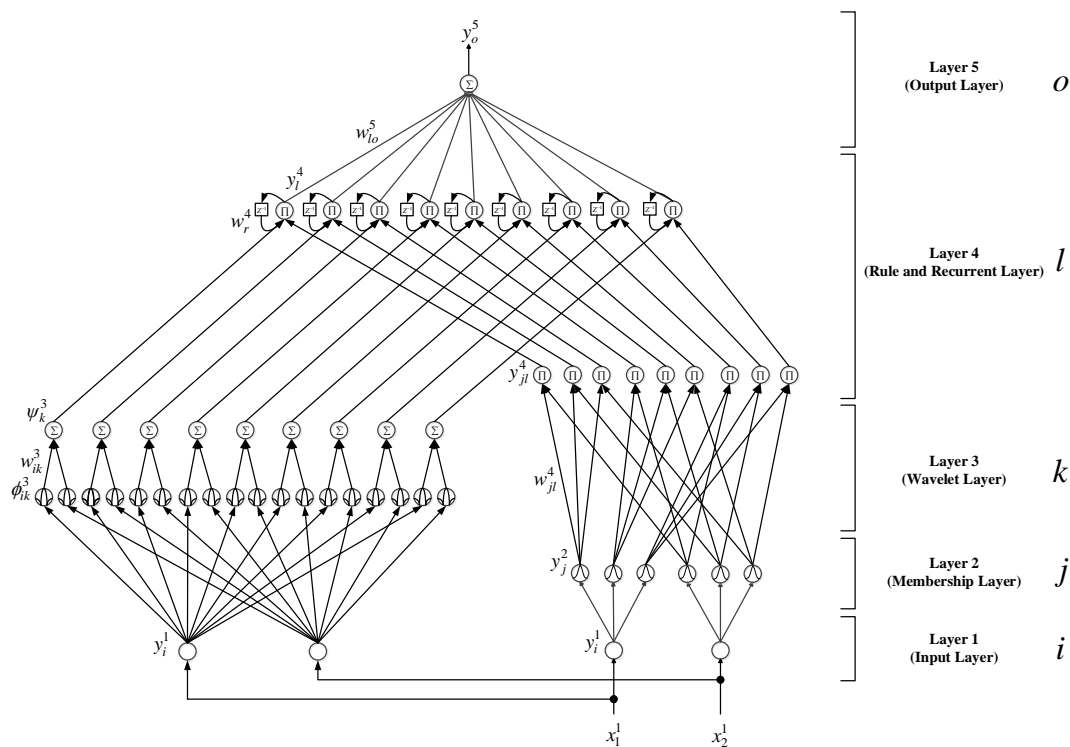


Figure 8. Network structure of RWFNN.

Figure 9 illustrates the flowchart outlining the proposed RWFNN controller. The detailed description of the operational mechanisms in the proposed RWFNN is as follows:

1. Measuring:

Utilizing the eQEP module in the DSP, the position response is measured with the assistance of an incremental encoder that has a resolution of 2500 counts/rev. Then, the RWFNN controller receives and utilizes  $e_1 = \theta_r^*(t) - \theta_r(t)$  and  $e_2 = \omega_r(t) + \lambda_1$  for generating control signals.

2. RWFNN Input Layer:

Two input signals are fed into this layer of the proposed RWFNN controller: the tracking error of the rotor position  $x_1^1 = e_1$  and the virtual control error  $x_2^1 = e_2$ . To describe the input and output of each node  $i$  in this layer, the following expression is used:

$$net_i^1(N) = x_i^1(N) \tag{29}$$

$$y_i^1(N) = f_i^1\left(net_i^1(N)\right) = net_i^1(N), \quad i = 1, 2 \tag{30}$$

The network inputs are represented by  $net_i^1(N)$ , where the superscript and subscript correspond to the layer and node numbers, respectively.  $N$  denotes the sampling iteration number, while  $y_i^1(N)$  is the output of node  $i$ th. The unity function is denoted as  $f_i^1(\cdot)$ .

3. RWFNN Membership Layer:

Layer 2 takes the outputs of layer 1 as its inputs. Additionally, the membership function utilized in this layer is the Gaussian function. The following elucidate the correlation between the input and output of each node in a comprehensive manner:

$$net_j^2(N) = -\frac{\left(x_i^2(N) - m_j^2\right)^2}{\left(\sigma_j^2\right)^2} \tag{31}$$

$$y_j^2(N) = f_j^2\left(\text{net}_j^2(N)\right) = \exp(\text{net}_j^2(N)), j = 1, 2, \dots, 6 \quad (32)$$

The input is denoted by  $x_i^2(N) = y_i^1(N)$ ; the mean and standard deviation of the Gaussian function for node  $j$ th are represented by  $m_j^2$  and  $\sigma_j^2$  respectively; the output of node  $j$ th is denoted by  $y_j^2(N)$ ;  $f_j^2(\cdot)$  is an exponential function.

#### 4. RWFNN Wavelet Layer:

The propagation of signals in the wavelet layer is illustrated below:

$$\phi_{ik}^3(x) = \frac{1}{\sqrt{|\sigma_{ik}^3|}} \left[ 1 - \frac{(x_i^1(N) - m_{ik}^3)^2}{(\sigma_{ik}^3)^2} \right] \times \exp \left[ -\frac{(x_i^1(N) - m_{ik}^3)^2}{(\sigma_{ik}^3)^2} \right], k = 1, 2, \dots, 9 \quad (33)$$

$$\psi_k^3(N) = \sum w_{ik}^3 \phi_{ik}^3(x) \quad (34)$$

The input to node  $i$ th from layer 1, directed towards the wavelet function of node  $k$ th, is represented as  $\phi_{ik}^3$ , and the connective weight as  $w_{ik}^3$ . In the wavelet layer, the output of node  $k$ th is represented by  $\psi_k^3$ . The dilation and translation variables of the wavelet function are expressed as  $m_{ik}^3$  and  $\sigma_{ik}^3$ , respectively.

#### 5. RWFNN Rule and Recurrent Layer:

The layer comprises a rule layer and a recurrent layer. Each node  $l$ , denoted as  $\Pi$ , performs a multiplication operation on the input signals and outputs their product. Additionally, the nodes in the rule and recurrent layer employ a multiplication operation on the output signals derived from the membership layer, wavelet layer, and recurrent layer. This dynamic mapping process enhances the overall mapping capability of the system. The nodes are summarized as follows:

$$y_{jl}^4(N) = \prod w_{jl}^4 y_j^2, l = 1, 2, \dots, 9 \quad (35)$$

$$\text{net}_l^4(N) = y_{jl}^4 \psi_k^3 w_r^4 y_l^4(N-1) \quad (36)$$

$$y_l^4(N) = f_l^4\left(\text{net}_l^4(N)\right) = \text{net}_l^4(N) \quad (37)$$

The output of the  $l$ th node in this layer is represented by  $y_l^4(N)$ . The calculation involves the utilization of the connecting weight, denoted as  $w_{jl}^4$ , between layer 2 and layer 4, and the recurrent weight is denoted by  $w_r^4$ .  $y_l^4(N-1)$  denotes the previous output of node  $l$ th in this layer, and the unity function is denoted as  $f_l^4(\cdot)$ . Each node in the network incorporates a feedback loop using the recurrent technique to achieve dynamic mapping and higher sensitivity to previously obtained data.

#### 6. RWFNN Output Layer:

The inputs to layer 5 are obtained from the outputs of layer 4 and compute the final output by summing them up. In this layer, the output  $y_o^5(N)$  is mathematically expressed as follows:

$$\text{net}_o^5(N) = \sum_l^9 w_{lo}^5 x_l^4(N), o = 1 \quad (38)$$

$$y_o^5(N) = f_o^5\left(\text{net}_o^5(N)\right) = \text{net}_o^5(N) \quad (39)$$

The output of the rule layer is represented as  $x_l^5(N) = y_l^4(N)$ . The connective weight is represented by  $w_{lo}^5$ . The final output of the RWFNN is depicted as  $y_o^5(N)$ . The unity function is denoted as  $f_o^5(\cdot)$ .

7. Online Network Parameters Learning:

All the adaptation laws of online network parameters learning will be given in Theorem 1 in the following section.

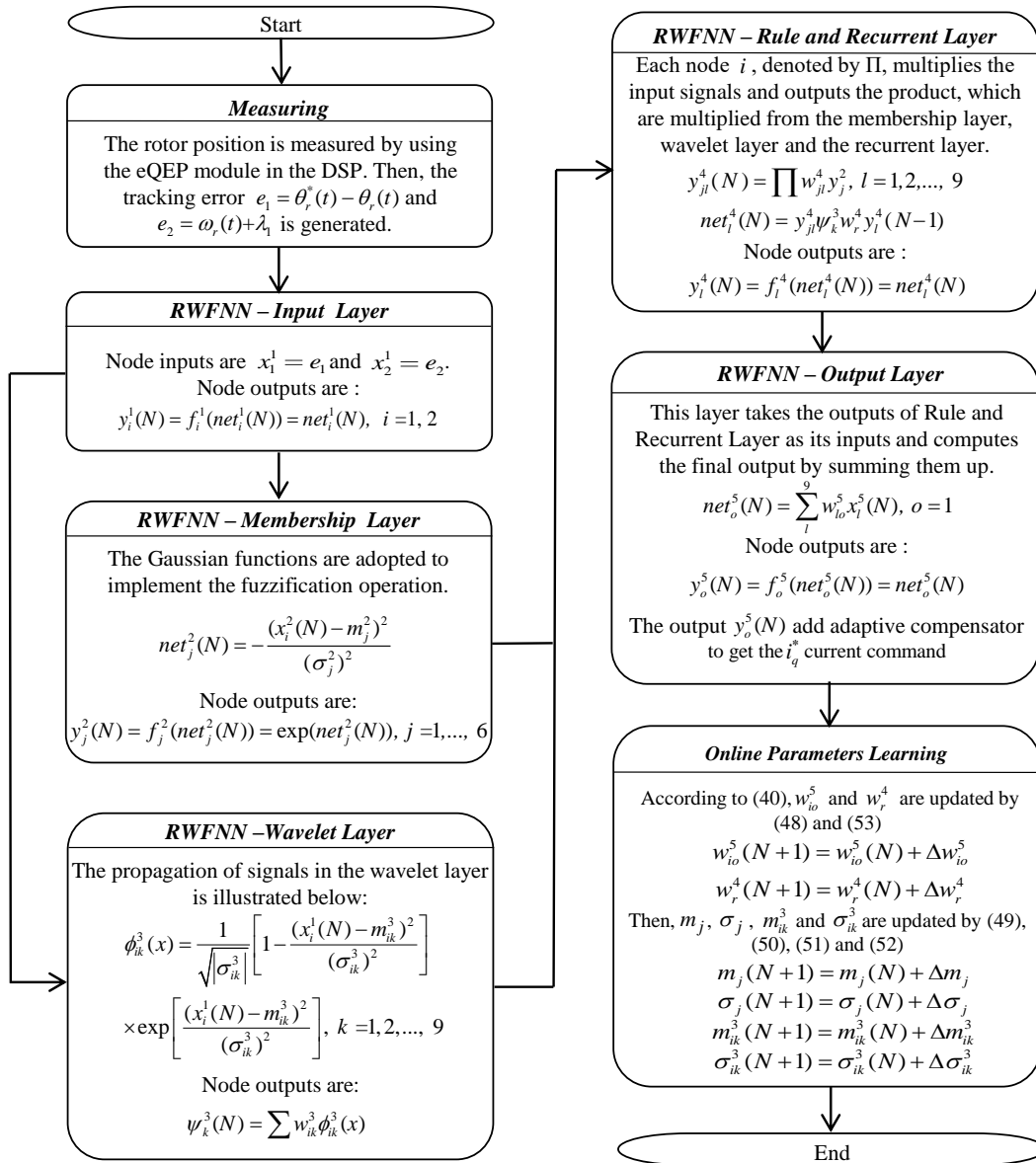


Figure 9. RWFNN flowchart for position control.

5. Stability Analysis of IBSCRWFNN System

The structure of the five-layer RWFNN, as illustrated in Figure 8, can be expressed as

$$\begin{aligned}
 U_{RWFNN}(e_1, e_2, W, m_j, \sigma_j, m_{ik}, \sigma_{ik}, R) &\equiv WT \\
 W = [w_1^5 w_2^5 w_3^5 w_4^5 w_5^5 w_6^5 w_7^5 w_8^5 w_9^5] &\in R^{1 \times 9} & \Gamma = [x_1^5 x_2^5 x_3^5 x_4^5 x_5^5 x_6^5 x_7^5 x_8^5 x_9^5]^T &\in R^{9 \times 1} \\
 m_j = [m_1^2 m_2^2 m_3^2 m_4^2 m_5^2 m_6^2]^T &\in R^{6 \times 1} & \sigma_j = [\sigma_1^2 \sigma_2^2 \sigma_3^2 \sigma_4^2 \sigma_5^2 \sigma_6^2]^T &\in R^{6 \times 1} \\
 m_{ik} = [m_1^3 m_2^3 \dots m_{18}^3]^T &\in R^{18 \times 1} & \sigma_{ik} = [\sigma_1^3 \sigma_2^3 \dots \sigma_{18}^3]^T &\in R^{18 \times 1} \\
 R = [w_{r1}^4 w_{r2}^4 w_{r3}^4 w_{r4}^4 w_{r5}^4 w_{r6}^4 w_{r7}^4 w_{r8}^4 w_{r9}^4] &\in R^{1 \times 9}
 \end{aligned} \tag{40}$$

The universal approximation property guarantees the existence of an optimal  $U_{RWFNN}^*$  for any nonlinear function. Consequently, a designed optimal  $U_{RWFNN}^*$  is employed to learn the BSC law  $U_{BSC}$  in order to achieve the following:

$$U_{BSC} = U_{RWFNN}^*(e_1, e_2, \mathbf{W}^*, \mathbf{m}_j^*, \sigma_j^*, \mathbf{m}_{ik}^*, \sigma_{ik}^*, \mathbf{R}^*) + \varepsilon = \mathbf{W}^* \mathbf{\Gamma}^* + \varepsilon \tag{41}$$

The reconstructed error is represented by  $\varepsilon$ , which is the minimum value;  $\mathbf{W}^*$ ,  $\mathbf{m}_j^*$ ,  $\sigma_j^*$ ,  $\mathbf{m}_{ik}^*$ ,  $\sigma_{ik}^*$ , and  $\mathbf{R}^*$  are the optimal values of  $\mathbf{W}$ ,  $\mathbf{m}_j$ ,  $\sigma_j$ ,  $\mathbf{m}_{ik}$ ,  $\sigma_{ik}$ , and  $\mathbf{R}$  respectively. Additionally, the control law illustrated in Equation (28) can be expressed as

$$U = \hat{U}_{RWFNN}(e_1, e_2, \hat{\mathbf{W}}, \hat{\mathbf{m}}_j, \hat{\sigma}_j, \hat{\mathbf{m}}_{ik}, \hat{\sigma}_{ik}, \hat{\mathbf{R}}) + \hat{U}_c = \hat{\mathbf{W}} \hat{\mathbf{\Gamma}} + \hat{U}_c \tag{42}$$

where  $\hat{\mathbf{W}}$ ,  $\hat{\mathbf{m}}_j$ ,  $\hat{\sigma}_j$ ,  $\hat{\mathbf{m}}_{ik}$ ,  $\hat{\sigma}_{ik}$ , and  $\hat{\mathbf{R}}$  represent the estimated values of  $\mathbf{W}$ ,  $\mathbf{m}_j$ ,  $\sigma_j$ ,  $\mathbf{m}_{ik}$ ,  $\sigma_{ik}$ , and  $\mathbf{R}$  correspondingly. The equation below is obtained by subtracting (41) from (42):

$$\begin{aligned} \tilde{U} &= U_{BSC} - U \\ &= U_{BSC} - \hat{U}_{RWFNN}(e_1, e_2, \hat{\mathbf{W}}, \hat{\mathbf{m}}_j, \hat{\sigma}_j, \hat{\mathbf{m}}_{ik}, \hat{\sigma}_{ik}, \hat{\mathbf{R}}) - \hat{U}_c \\ &= U_{RWFNN}^*(e_1, e_2, \mathbf{W}^*, \mathbf{m}_j^*, \sigma_j^*, \mathbf{m}_{ik}^*, \sigma_{ik}^*, \mathbf{R}^*) + \varepsilon \\ &\quad - \hat{U}_{RWFNN}(e_1, e_2, \hat{\mathbf{W}}, \hat{\mathbf{m}}_j, \hat{\sigma}_j, \hat{\mathbf{m}}_{ik}, \hat{\sigma}_{ik}, \hat{\mathbf{R}}) - \hat{U}_c \\ &= \mathbf{W}^* \mathbf{\Gamma}^* + \varepsilon - \hat{\mathbf{W}} \hat{\mathbf{\Gamma}} - \hat{U}_c \\ &= \tilde{\mathbf{W}} \mathbf{\Gamma}^* + \tilde{\mathbf{W}} \hat{\mathbf{\Gamma}} + \varepsilon - \hat{U}_c \end{aligned} \tag{43}$$

where  $\tilde{\mathbf{W}} = \mathbf{W}^* - \hat{\mathbf{W}}$  and  $\tilde{\mathbf{\Gamma}} = \mathbf{\Gamma}^* - \hat{\mathbf{\Gamma}}$ . A linearization technique is employed to convert the RWFNN into a partially linear form. This technique involves obtaining the Taylor series expansion of  $\tilde{\mathbf{\Gamma}}$ , which can be expressed as

$$\tilde{\mathbf{\Gamma}} = \mathbf{\Gamma}_{m_j}^T \tilde{\mathbf{m}}_j + \mathbf{\Gamma}_{\sigma_j}^T \tilde{\sigma}_j + \mathbf{\Gamma}_{m_{ik}}^T \tilde{\mathbf{m}}_{ik} + \mathbf{\Gamma}_{\sigma_{ik}}^T \tilde{\sigma}_{ik} + \mathbf{\Gamma}_R^T \tilde{\mathbf{R}} + N_h \tag{44}$$

where  $\tilde{\mathbf{m}}_j = \mathbf{m}_j^* - \hat{\mathbf{m}}_j$ ,  $\tilde{\sigma}_j = \sigma_j^* - \hat{\sigma}_j$ ,  $\tilde{\mathbf{m}}_{ik} = \mathbf{m}_{ik}^* - \hat{\mathbf{m}}_{ik}$ ,  $\tilde{\sigma}_{ik} = \sigma_{ik}^* - \hat{\sigma}_{ik}$ ,  $\tilde{\mathbf{R}} = \mathbf{R}^* - \hat{\mathbf{R}}$ ; the high-order term is represented by  $N_h$ . In addition,

$$\begin{aligned} \mathbf{\Gamma}_{m_j}^T &= \begin{bmatrix} \frac{\partial x_1^5}{\partial m_1} & \frac{\partial x_1^5}{\partial m_2} & \dots & \frac{\partial x_1^5}{\partial m_6} \\ \frac{\partial x_2^5}{\partial m_1} & \frac{\partial x_2^5}{\partial m_2} & \dots & \frac{\partial x_2^5}{\partial m_6} \\ \vdots & \vdots & \ddots & \vdots \\ \frac{\partial x_9^5}{\partial m_1} & \frac{\partial x_9^5}{\partial m_2} & \dots & \frac{\partial x_9^5}{\partial m_6} \end{bmatrix} \in R^{9 \times 6} & \quad \mathbf{\Gamma}_{\sigma_j}^T &= \begin{bmatrix} \frac{\partial x_1^5}{\partial \sigma_1} & \frac{\partial x_1^5}{\partial \sigma_2} & \dots & \frac{\partial x_1^5}{\partial \sigma_6} \\ \frac{\partial x_2^5}{\partial \sigma_1} & \frac{\partial x_2^5}{\partial \sigma_2} & \dots & \frac{\partial x_2^5}{\partial \sigma_6} \\ \vdots & \vdots & \ddots & \vdots \\ \frac{\partial x_9^5}{\partial \sigma_1} & \frac{\partial x_9^5}{\partial \sigma_2} & \dots & \frac{\partial x_9^5}{\partial \sigma_6} \end{bmatrix} \in R^{9 \times 6} \\ \mathbf{\Gamma}_{m_{ik}}^T &= \begin{bmatrix} \frac{\partial x_1^5}{\partial m_1} & \frac{\partial x_1^5}{\partial m_2} & \dots & \frac{\partial x_1^5}{\partial m_{18}} \\ \frac{\partial x_2^5}{\partial m_1} & \frac{\partial x_2^5}{\partial m_2} & \dots & \frac{\partial x_2^5}{\partial m_{18}} \\ \vdots & \vdots & \ddots & \vdots \\ \frac{\partial x_9^5}{\partial m_1} & \frac{\partial x_9^5}{\partial m_2} & \dots & \frac{\partial x_9^5}{\partial m_{18}} \end{bmatrix} \in R^{9 \times 18} & \quad \mathbf{\Gamma}_{\sigma_{ik}}^T &= \begin{bmatrix} \frac{\partial x_1^5}{\partial \sigma_1} & \frac{\partial x_1^5}{\partial \sigma_2} & \dots & \frac{\partial x_1^5}{\partial \sigma_{18}} \\ \frac{\partial x_2^5}{\partial \sigma_1} & \frac{\partial x_2^5}{\partial \sigma_2} & \dots & \frac{\partial x_2^5}{\partial \sigma_{18}} \\ \vdots & \vdots & \ddots & \vdots \\ \frac{\partial x_9^5}{\partial \sigma_1} & \frac{\partial x_9^5}{\partial \sigma_2} & \dots & \frac{\partial x_9^5}{\partial \sigma_{18}} \end{bmatrix} \in R^{9 \times 18} \\ \mathbf{\Gamma}_R^T &= \begin{bmatrix} \frac{\partial x_1^5}{\partial w_{r1}} & \frac{\partial x_1^5}{\partial w_{r2}} & \dots & \frac{\partial x_1^5}{\partial w_{r9}} \\ \frac{\partial x_2^5}{\partial w_{r1}} & \frac{\partial x_2^5}{\partial w_{r2}} & \dots & \frac{\partial x_2^5}{\partial w_{r9}} \\ \vdots & \vdots & \ddots & \vdots \\ \frac{\partial x_9^5}{\partial w_{r1}} & \frac{\partial x_9^5}{\partial w_{r2}} & \dots & \frac{\partial x_9^5}{\partial w_{r9}} \end{bmatrix} \in R^{9 \times 9} \end{aligned}$$

Rewriting (44),  $\Gamma^*$  can be calculated as follows:

$$\Gamma^* = \hat{\Gamma} + \tilde{\Gamma} = \hat{\Gamma} + \Gamma_{m_j}^T \tilde{m}_j + \Gamma_{\sigma_j}^T \tilde{\sigma}_j + \Gamma_{m_{ik}}^T \tilde{m}_{ik} + \Gamma_{\sigma_{ik}}^T \tilde{\sigma}_{ik} + \Gamma_R^T \tilde{R} + N_h \quad (45)$$

Substituting (44) and (45) into (43), expressing the estimated error in Equation (46) can be performed in the following manner:

$$\begin{aligned} \tilde{U} &= \tilde{W}\Gamma^* + \hat{W}\tilde{\Gamma} + \varepsilon - \hat{U}_c \\ &= \tilde{W}(\hat{\Gamma} + \Gamma_{m_j}^T \tilde{m}_j + \Gamma_{\sigma_j}^T \tilde{\sigma}_j + \Gamma_{m_{ik}}^T \tilde{m}_{ik} + \Gamma_{\sigma_{ik}}^T \tilde{\sigma}_{ik} + \Gamma_R^T \tilde{R} + N_h) \\ &\quad + \hat{W}(\Gamma_{m_j}^T \tilde{m}_j + \Gamma_{\sigma_j}^T \tilde{\sigma}_j + \Gamma_{m_{ik}}^T \tilde{m}_{ik} + \Gamma_{\sigma_{ik}}^T \tilde{\sigma}_{ik} + \Gamma_R^T \tilde{R} + N_h) + \varepsilon - \hat{U}_c \\ &= \tilde{W}\hat{\Gamma} + \tilde{W}\Gamma_{m_j}^T \tilde{m}_j + \tilde{W}\Gamma_{\sigma_j}^T \tilde{\sigma}_j + \tilde{W}\Gamma_{m_{ik}}^T \tilde{m}_{ik} + \tilde{W}\Gamma_{\sigma_{ik}}^T \tilde{\sigma}_{ik} + \tilde{W}\Gamma_R^T \tilde{R} + \tilde{W}N_h \\ &\quad + \hat{W}\Gamma_{m_j}^T \tilde{m}_j + \hat{W}\Gamma_{\sigma_j}^T \tilde{\sigma}_j + \hat{W}\Gamma_{m_{ik}}^T \tilde{m}_{ik} + \hat{W}\Gamma_{\sigma_{ik}}^T \tilde{\sigma}_{ik} + \hat{W}\Gamma_R^T \tilde{R} + \hat{W}N_h + \varepsilon - \hat{U}_c \\ &= \tilde{W}\hat{\Gamma} + \hat{W}\Gamma_{m_j}^T \tilde{m}_j + \hat{W}\Gamma_{\sigma_j}^T \tilde{\sigma}_j + \hat{W}\Gamma_{m_{ik}}^T \tilde{m}_{ik} + \hat{W}\Gamma_{\sigma_{ik}}^T \tilde{\sigma}_{ik} + \hat{W}\Gamma_R^T \tilde{R} + \tilde{W}\Gamma_{m_j}^T \tilde{m}_j \\ &\quad + \tilde{W}\Gamma_{\sigma_j}^T \tilde{\sigma}_j + \tilde{W}\Gamma_{m_{ik}}^T \tilde{m}_{ik} + \tilde{W}\Gamma_{\sigma_{ik}}^T \tilde{\sigma}_{ik} + \tilde{W}\Gamma_R^T \tilde{R} + W^*N_h + \varepsilon - \hat{U}_c \\ &= \tilde{W}\hat{\Gamma} + \hat{W}\Gamma_{m_j}^T \tilde{m}_j + \hat{W}\Gamma_{\sigma_j}^T \tilde{\sigma}_j + \hat{W}\Gamma_{m_{ik}}^T \tilde{m}_{ik} + \hat{W}\Gamma_{\sigma_{ik}}^T \tilde{\sigma}_{ik} + \hat{W}\Gamma_R^T \tilde{R} - \hat{U}_c + H \end{aligned} \quad (46)$$

The  $H$ , which is named as the uncertain term, can be expressed as follows:

$$H = \tilde{W}\Gamma_{m_j}^T \tilde{m}_j + \tilde{W}\Gamma_{\sigma_j}^T \tilde{\sigma}_j + \tilde{W}\Gamma_{m_{ik}}^T \tilde{m}_{ik} + \tilde{W}\Gamma_{\sigma_{ik}}^T \tilde{\sigma}_{ik} + \tilde{W}\Gamma_R^T \tilde{R} + W^*N_h + \varepsilon \quad (47)$$

**Theorem 1.** Given the PMASynRM servo drive system described in (12), the proposed IBSCR-WFNN achieves absolute asymptotic stability under the following condition.

1. Implementation of the IBSCRWFNN control as illustrated in (28);
2. Adoption of the RWFNN adaptation law as described in (48)–(53);
3. The compensators, illustrated in Equations (54) and (55), are developed with an adaptive law.

$$\dot{\hat{W}}^T = -\eta_w e_2 \hat{\Gamma} \quad (48)$$

$$\dot{\hat{m}}_j^T = -\eta_{m_j} e_2 \hat{W}\Gamma_{m_j}^T \quad (49)$$

$$\dot{\hat{\sigma}}_j^T = -\eta_{\sigma_j} e_2 \hat{W}\Gamma_{\sigma_j}^T \quad (50)$$

$$\dot{\hat{m}}_{ik}^T = -\eta_{m_{ik}} e_2 \hat{W}\Gamma_{m_{ik}}^T \quad (51)$$

$$\dot{\hat{\sigma}}_{ik}^T = -\eta_{\sigma_{ik}} e_2 \hat{W}\Gamma_{\sigma_{ik}}^T \quad (52)$$

$$\dot{\hat{R}}^T = -\eta_r e_2 \hat{W}\Gamma_R^T \quad (53)$$

$$\hat{U}_c = \hat{\psi} \quad (54)$$

$$\dot{\hat{\psi}} = -\gamma e_2 \quad (55)$$

where  $\eta_w, \eta_{m_j}, \eta_{\sigma_j}, \eta_{m_{ik}}, \eta_{\sigma_{ik}}, \eta_r$  are positive constant learning rate parameters;  $\hat{\psi}$  represents the value of the estimated online approximated error; and  $\gamma$  is a positive constant.

**Proof.** The proposed IBSCRWFNN is designed with a Lyapunov function given by

$$\begin{aligned}
 &V_3(e_1(t), e_2(t), \tilde{\psi}(t), \tilde{W}, \tilde{m}_j, \tilde{\sigma}_j, \tilde{m}_{ik}, \tilde{\sigma}_{ik}, \tilde{R}) \\
 &= \frac{1}{2}e_1^2 + \frac{1}{2}e_2^2 + \frac{B_m}{2\eta_w} \tilde{W}\tilde{W}^T + \frac{B_m}{2\eta_{m_j}} \tilde{m}_j^T \tilde{m}_j + \frac{B_m}{2\eta_{\sigma_j}} \tilde{\sigma}_j^T \tilde{\sigma}_j \\
 &+ \frac{B_m}{2\eta_{m_{ik}}} \tilde{m}_{ik}^T \tilde{m}_{ik} + \frac{B_m}{2\eta_{\sigma_{ik}}} \tilde{\sigma}_{ik}^T \tilde{\sigma}_{ik} + \frac{B_m}{2\eta_r} \tilde{R}^T \tilde{R} + \frac{B_m}{2\gamma} \|\tilde{\psi}\|^2 > 0
 \end{aligned} \tag{56}$$

The function  $V_3$  is chosen to be positive-definite, and  $\tilde{\psi} = \psi - \hat{\psi}$ .  $\psi$  is the symbol used to denote the approximated error, and it is defined by  $\psi = H - F/B_m$ . Furthermore, the approximated error  $\psi$  is assumed to be bounded by  $|\psi| \leq F_b$ . Given that the sampling interval in the experiment is considerably shorter than the fluctuations observed in  $H$  and  $F$ , the approximated error  $\psi$  is treated as a constant during the estimation process. However, it is difficult to know the upper bound  $F_b$ . Hence, a proposed adaptation law is put forth to modify the value of the online estimated approximated error  $\tilde{\psi}$  within the compensator. Differentiating  $\tilde{\psi}$  with respect to time yields  $\dot{\tilde{\psi}} = -\dot{\hat{\psi}}$ . By utilizing Equation (12) and taking the derivative of  $V_3$  with respect to time, the following expression can be derived:

$$\begin{aligned}
 \dot{V}_3 &= e_1\dot{e}_1 + e_2\dot{e}_2 - \frac{B_m}{\eta_w} \tilde{W}\dot{W}^T - \frac{B_m}{\eta_{m_j}} \dot{m}_j^T \tilde{m}_j - \frac{B_m}{\eta_{\sigma_j}} \dot{\sigma}_j^T \tilde{\sigma}_j - \frac{B_m}{\eta_{m_{ik}}} \dot{m}_{ik}^T \tilde{m}_{ik} - \frac{B_m}{\eta_{\sigma_{ik}}} \dot{\sigma}_{ik}^T \tilde{\sigma}_{ik} - \frac{B_m}{\eta_r} \dot{R}^T \tilde{R} - \frac{B_m}{\gamma} \tilde{\psi} \dot{\tilde{\psi}} \\
 &= e_1[-e_2 - c_1e_1] - e_2\{B_m[U_{BSC} - U] - e_1 + c_2e_2 - F\} - \frac{B_m}{\eta_w} \tilde{W}\dot{W}^T \\
 &- \frac{B_m}{\eta_{m_j}} \dot{m}_j^T \tilde{m}_j - \frac{B_m}{\eta_{\sigma_j}} \dot{\sigma}_j^T \tilde{\sigma}_j - \frac{B_m}{\eta_{m_{ik}}} \dot{m}_{ik}^T \tilde{m}_{ik} - \frac{B_m}{\eta_{\sigma_{ik}}} \dot{\sigma}_{ik}^T \tilde{\sigma}_{ik} - \frac{B_m}{\eta_r} \dot{R}^T \tilde{R} - \frac{B_m}{\gamma} \tilde{\psi} \dot{\tilde{\psi}} \\
 &= -c_1e_1^2 - c_2e_2^2 - \frac{B_m}{\eta_w} \tilde{W}\dot{W}^T - e_2B_m\tilde{W}\dot{W}^T - \frac{B_m}{\eta_{m_j}} \dot{m}_j^T \tilde{m}_j - e_2B_m\dot{W}\Gamma_{m_j}^T \tilde{m}_j - \frac{B_m}{\eta_{\sigma_j}} \dot{\sigma}_j^T \tilde{\sigma}_j \\
 &- e_2B_m\dot{W}\Gamma_{\sigma_j}^T \tilde{\sigma}_j - \frac{B_m}{\eta_{m_{ik}}} \dot{m}_{ik}^T \tilde{m}_{ik} - e_2B_m\dot{W}\Gamma_{m_{ik}}^T \tilde{m}_{ik} - \frac{B_m}{\eta_{\sigma_{ik}}} \dot{\sigma}_{ik}^T \tilde{\sigma}_{ik} - e_2B_m\dot{W}\Gamma_{\sigma_{ik}}^T \tilde{\sigma}_{ik} \\
 &- \frac{B_m}{\eta_r} \dot{R}^T \tilde{R} - e_2B_m\dot{W}\Gamma_R^T \tilde{R} + e_2B_m\dot{U}_c - e_2B_m\dot{\psi} - \frac{B_m}{\gamma} \tilde{\psi} \dot{\tilde{\psi}} \\
 &= -c_1e_1^2 - c_2e_2^2 - \left[ \frac{B_m}{\eta_w} \tilde{W}\dot{W}^T + e_2B_m\tilde{W}\dot{W}^T \right] - \left[ \frac{B_m}{\eta_{m_j}} \dot{m}_j^T \tilde{m}_j + e_2B_m\dot{W}\Gamma_{m_j}^T \tilde{m}_j \right] - \left[ \frac{B_m}{\eta_{\sigma_j}} \dot{\sigma}_j^T \tilde{\sigma}_j + e_2B_m\dot{W}\Gamma_{\sigma_j}^T \tilde{\sigma}_j \right] \\
 &- \left[ \frac{B_m}{\eta_{m_{ik}}} \dot{m}_{ik}^T \tilde{m}_{ik} + e_2B_m\dot{W}\Gamma_{m_{ik}}^T \tilde{m}_{ik} \right] - \left[ \frac{B_m}{\eta_{\sigma_{ik}}} \dot{\sigma}_{ik}^T \tilde{\sigma}_{ik} + e_2B_m\dot{W}\Gamma_{\sigma_{ik}}^T \tilde{\sigma}_{ik} \right] - \left[ \frac{B_m}{\eta_r} \dot{R}^T \tilde{R} + e_2B_m\dot{W}\Gamma_R^T \tilde{R} \right] \\
 &+ [e_2B_m\dot{U}_c - e_2B_m\dot{\psi}] - \frac{B_m}{\gamma} \tilde{\psi} [\dot{\tilde{\psi}} + \gamma e_2]
 \end{aligned} \tag{57}$$

Moreover, by substituting (48)–(55) into (57), it can be concluded that

$$\dot{V}_3(e_1(t), e_2(t), \tilde{\psi}(t), \tilde{W}, \tilde{m}_j, \tilde{\sigma}_j, \tilde{m}_{ik}, \tilde{\sigma}_{ik}, \tilde{R}) = -c_1e_1^2 - c_2e_2^2 \leq 0 \tag{58}$$

Since  $\dot{V}_3(e_1(t), e_2(t), \tilde{\psi}(t), \tilde{W}, \tilde{m}_j, \tilde{\sigma}_j, \tilde{m}_{ik}, \tilde{\sigma}_{ik}, \tilde{R}) \leq 0$  is negative semidefinite,

$$\dot{V}_3(e_1(t), e_2(t), \tilde{\psi}(t), \tilde{W}, \tilde{m}_j, \tilde{\sigma}_j, \tilde{m}_{ik}, \tilde{\sigma}_{ik}, \tilde{R}) < \dot{V}_3(e_1(0), e_2(0), \tilde{\psi}(0), \tilde{W}, \tilde{m}_j, \tilde{\sigma}_j, \tilde{m}_{ik}, \tilde{\sigma}_{ik}, \tilde{R})$$

which implies that  $e_1(t)$ ,  $e_2(t)$ ,  $\tilde{\psi}(t)$ ,  $\tilde{W}$ ,  $\tilde{m}_j$ ,  $\tilde{\sigma}_j$ ,  $\tilde{m}_{ik}$ ,  $\tilde{\sigma}_{ik}$ , and  $\tilde{R}$  are all bounded. By defining  $\Omega(t) = c_1e_1^2 + c_2e_2^2 = -\dot{V}_3(t)$  and integrating with respect to time, one can obtain the following equation:

$$\int_0^t \Omega(\tau) d\tau = V_3(0) - V_3(t) \tag{59}$$

Since  $\dot{V}_3(e_1(0), e_2(0), \tilde{\psi}(0), \tilde{W}, \tilde{m}_j, \tilde{\sigma}_j, \tilde{m}_{ik}, \tilde{\sigma}_{ik}, \tilde{R})$  is bounded and  $\dot{V}_3(e_1(t), e_2(t), \tilde{\psi}(t), \tilde{W}, \tilde{m}_j, \tilde{\sigma}_j, \tilde{m}_{ik}, \tilde{\sigma}_{ik}, \tilde{R})$  is also bounded and nonincreasing, thus

$$\lim_{t \rightarrow \infty} \int_0^t \Omega(\tau) d\tau < \infty \quad (60)$$

Furthermore, the boundedness of  $\dot{\Omega}(t)$  implies that  $\Omega(t)$  is uniformly continuous. Applying Barbalat's Lemma, it can be demonstrated that  $\lim_{t \rightarrow \infty} \Omega(t) \rightarrow 0$ . As a result, both  $e_1$  and  $e_2$  will approach zero as  $t \rightarrow \infty$ . Consequently, the proposed IBSCRWFNN system exhibits asymptotic stability [22].  $\square$

## 6. Experimentation

The experimental setup, depicted in Figure 10, comprises various components such as the PMASynRM servo drive, DSP TMS320F28075 board, and a SiC-based VSI with 4.5 kW. An industrial 7.5-kW PMSM drive is operated in torque control mode as the load. Moreover, two load torques 10 Nm (case 1) and 20 Nm (case 2), are set in the experimentation. The control of position and speed of the PMASynRM is determined using an incremental encoder, which interfaces with a quadrature encoder pulse (QEP) interface and has a sampling interval of 1 ms. The control of current operates with a sampling interval of 0.1 ms. The PMASynRM servo drive is then controlled by delivering switching commands for space vector pulse width modulation (SVPWM) to the voltage source inverter (VSI).

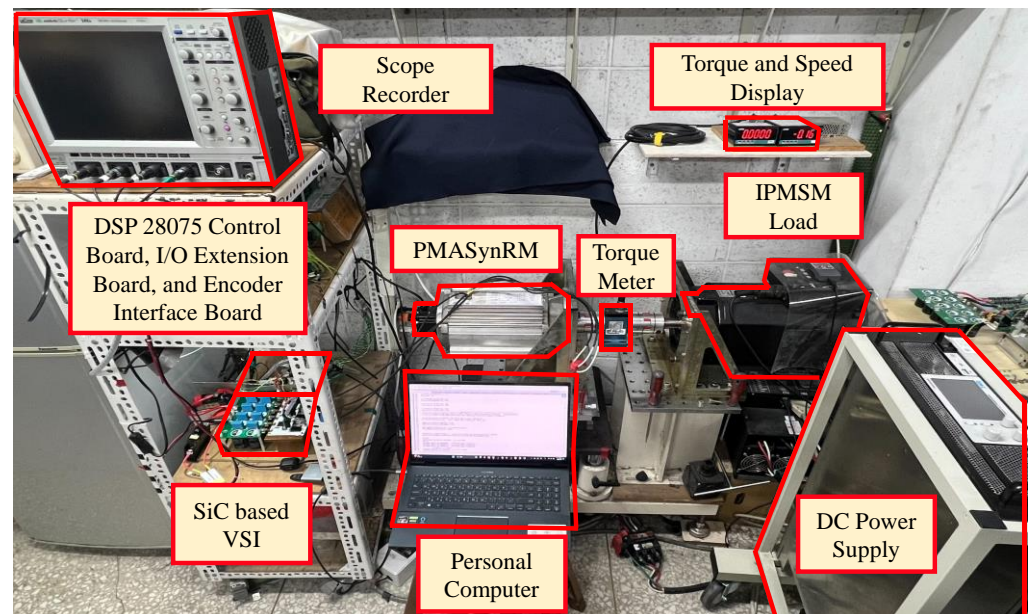


**Figure 10.** Experimental setup.

The suggested position control system is evaluated based on three performance metrics:  $T_M$ ,  $T_{aver}$ , and  $T_{sd}$ . These metrics represent the maximum tracking error, average tracking error, and standard deviation of the tracking error, respectively. They are utilized to assess and validate the control performance.

$$T_M = \max_N (|T_{error}(N)|) \quad (61)$$

$$T_{aver} = \frac{\sum_{N=1}^h |T_{error}(N)|}{h} \quad (62)$$

$$T_{sd} = \sqrt{\frac{\sum_{N=1}^h (T_{error}(N) - T_{aver}(N))^2}{h}} \quad (63)$$

Given that  $T_{error}(N) = \theta_r^*(N) - \theta_r(N)$  and  $h$  represents the total number of iterations, the control performance of the system is demonstrated by measuring the responses of periodical step and sinusoid commands. To model the periodical step reference input, a second-order transfer function with a rise time of 0.6 s is utilized as the reference model in the following:

$$\frac{\omega_n^2}{s^2 + 2\zeta\omega_n s + \omega_n^2} = \frac{30}{s^2 + 11s + 30} \quad (64)$$

In Equation (64),  $\zeta$  and  $\omega_n$  represent the damping ratio and undamped natural frequency, correspondingly. Moreover, the control performance of the proposed IBSCRWFNN position controller is compared with that of the BSC position controller through experimental results analysis. Furthermore, to compare the control performance, experimental results of the PI control, BSC, and the proposed IBSCRWFNN control are presented and analyzed. The parameters of PI control have been designed in Section 2.3, and the parameters of BSC and the proposed IBSCRWFNN control are provided as follows:

$$c_1 = 1.2, c_2 = 0.45, F_b = 10, \eta_w = 0.05, \eta_{m_j} = 0.15, \eta_{\sigma_j} = 0.3, \eta_{m_{ik}} = 0.01, \eta_{\sigma_{ik}} = 0.01, \eta_r = 0.02 \quad (65)$$

The parameters are iteratively adjusted to achieve optimal transient control performance while ensuring stability using a trial-and-error process. In addition, in order to strike a balance between computational resources and control performance, the network structure of the RWFNN has been designed with specific numbers of neurons in each layer: 2 in the input layer, 6 in the membership layer, 27 in the wavelet layer, 18 in the rule layer, and 1 in the output layer. Additionally, for the 32-bit floating-point DSP with 120 MHz using the “C” program, the total operation cycles and execution time for the PI controller are 60 and 0.0005 ms; the proposed BSC controller are 393 and 0.003275 ms; the proposed IBSCRWFNN controller are 9437 and 0.0786 ms. Consequently, the total execution time of the proposed IBSCRWFNN controller remains below 1 ms, which aligns with the sampling interval of the speed control loop.

In the experimentation, the objective is the control of the rotor position of PMASynRM to periodically track step and sinusoid position commands with minimum tracking errors. The test scenarios are outlined in Table 3 for the assessment of the robustness of various controllers under different operating conditions.

**Table 3.** Test scenarios and quantified results of experiment.

Case	Controller	Position Command (Degree)	Maximum Tracking Error (Degree)	Transient Response Time (s)	Load Torque (Nm)	Figure
Case 1	PI	periodical step	44.5	1.25	10	Figure 11a
Case 2	PI	periodical step	50.5	1.31	20	Figure 11c
Case 1	BSC	periodical step	28.3	1.15	10	Figure 12a
Case 2	BSC	periodical step	34	1.19	20	Figure 12c
Case 1	BSC	periodical sinusoid	13.2	0.82	10	Figure 13a
Case 2	BSC	periodical sinusoid	15	0.85	20	Figure 13c
Case 1	IBSCRWFNN	periodical step	14.5	0.62	10	Figure 14a
Case 2	IBSCRWFNN	periodical step	15.3	0.59	20	Figure 14c
Case 1	IBSCRWFNN	periodical sinusoid	4.9	0.32	10	Figure 15a
Case 2	IBSCRWFNN	periodical sinusoid	5.5	0.37	20	Figure 15c

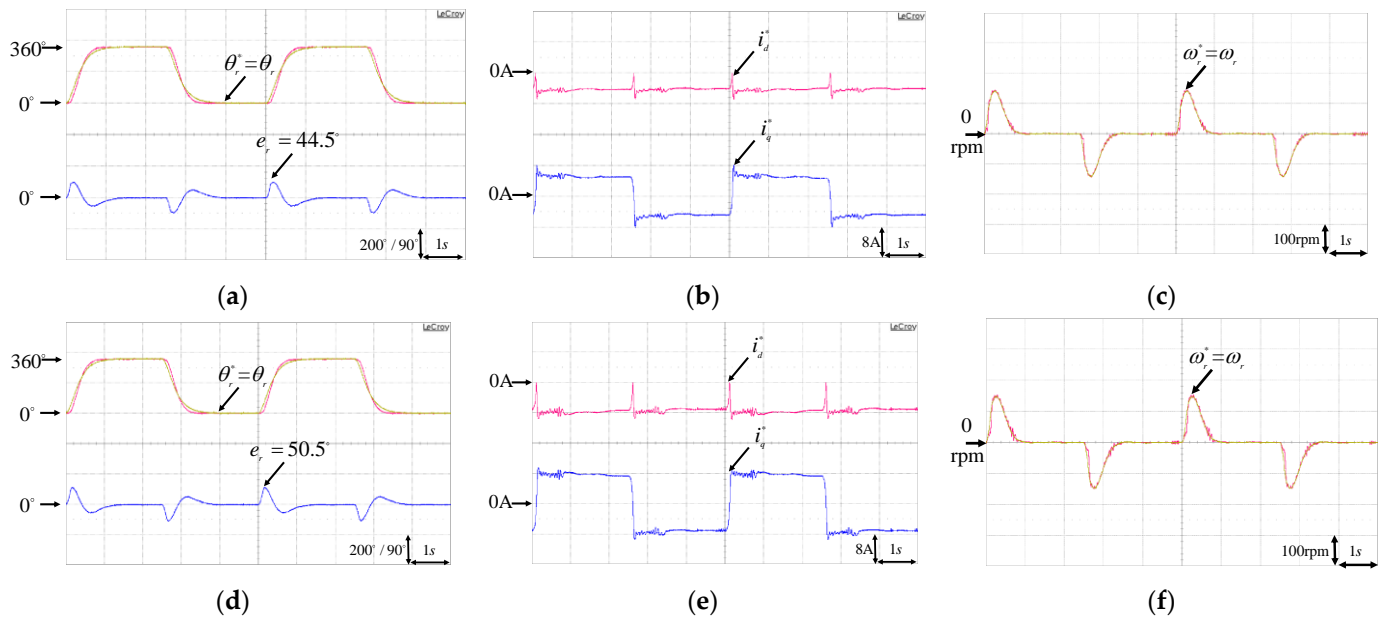


**Figure 11.** Experimental results of PI control with periodical step command. (a) Position command, response, and error at case 1; (b)  $d$ - $q$  axis current commands at case 1; (c) Speed command and response at case 1; (d) Position command, response, and error at case 2; (e)  $d$ - $q$  axis current commands at case 2; (f) Speed command and response at case 2.

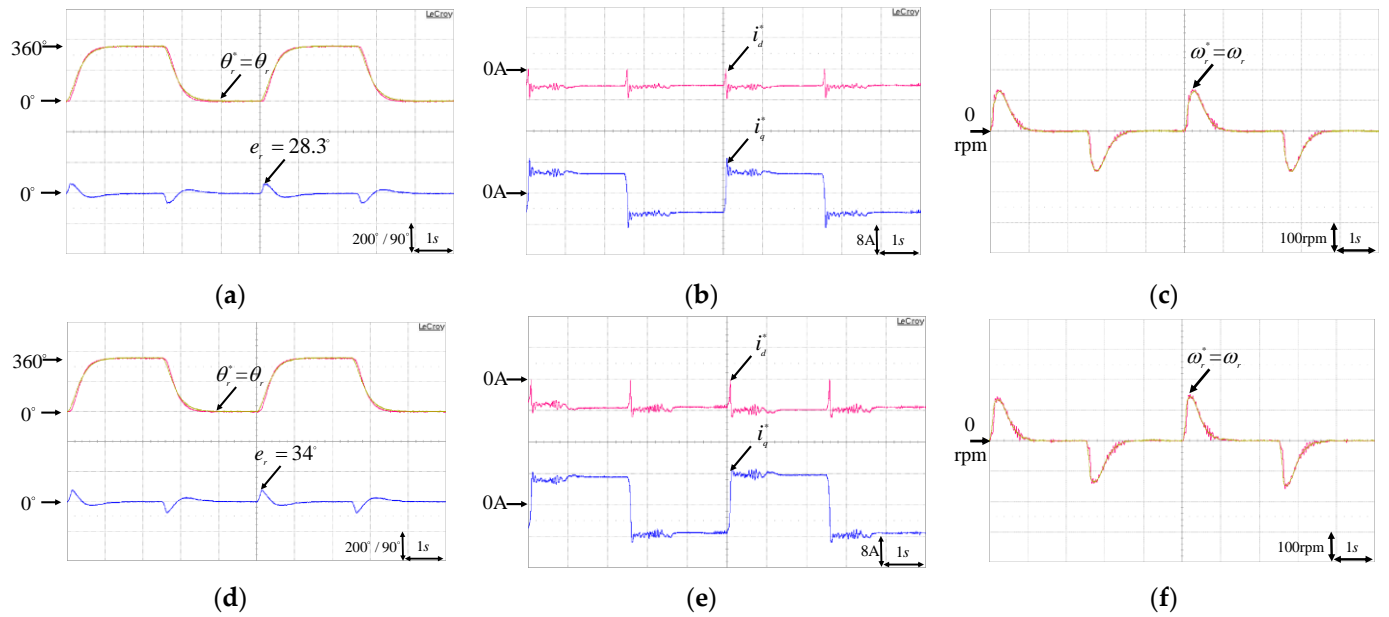


**Figure 12.** Experimental results of BSC control with periodical step command. (a) Position command, response, and error at case 1; (b)  $d$ - $q$  axis current commands at case 1; (c) Speed command and response at case 1; (d) Position command, response, and error at case 2; (e)  $d$ - $q$  axis current commands at case 2; (f) Speed command and response at case 2.

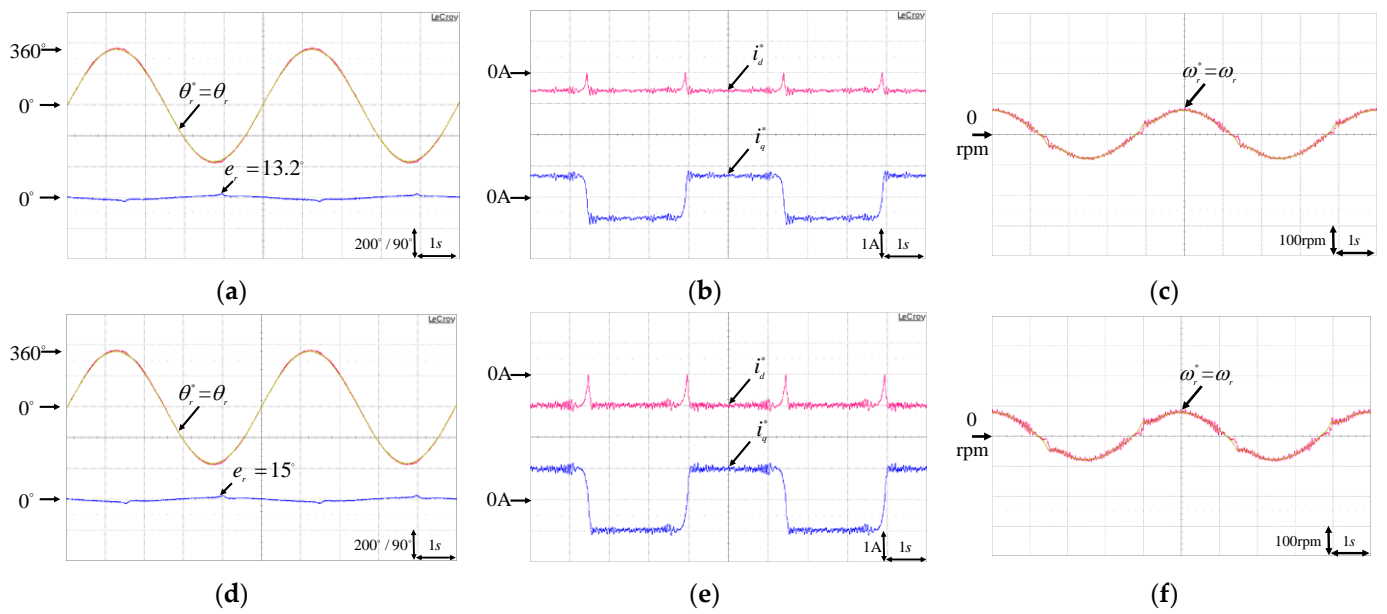


**Figure 13.** Experimental results of BSC control with periodical sinusoid command. (a) Position command, response, and error at case 1; (b)  $d$ - $q$  axis current commands at case 1; (c) Speed command and response at case 1; (d) Position command, response, and error at case 2; (e)  $d$ - $q$  axis current commands at case 2; (f) Speed command and response at case 2.

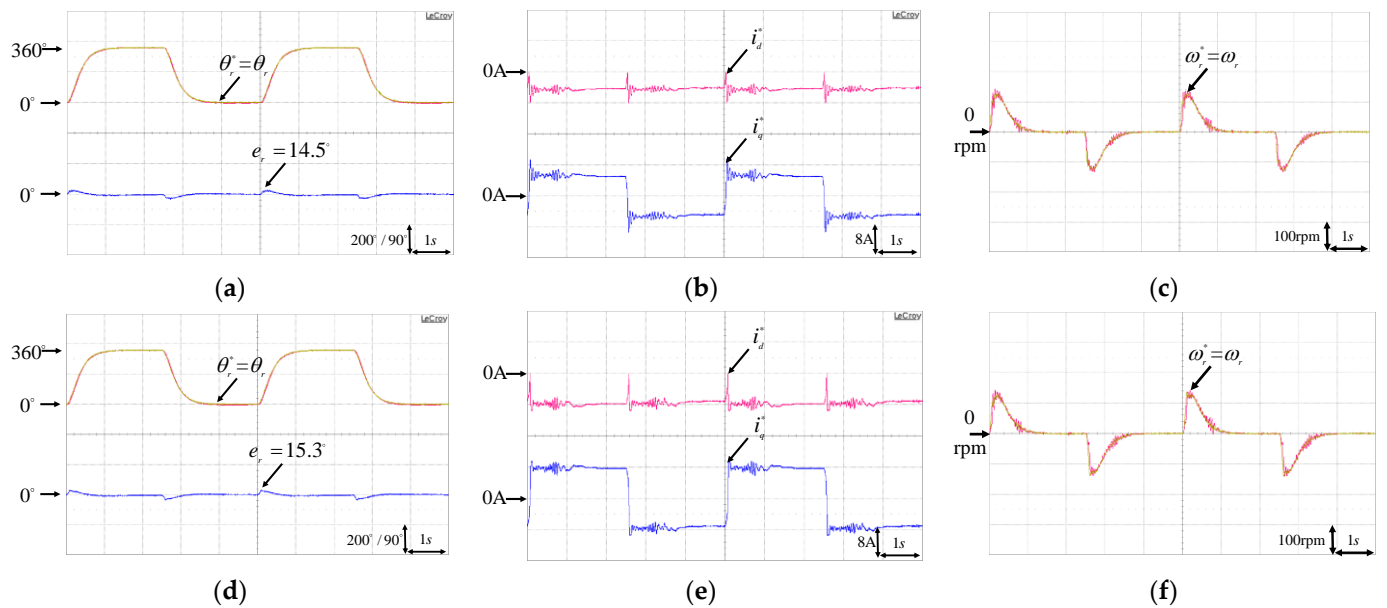


**Figure 14.** Experimental results of IBSCRWFNN control with periodical step command. (a) Position command, response, and error at case 1; (b)  $d$ - $q$  axis current commands at case 1; (c) Speed command and response at case 1; (d) Position command, response, and error at case 2; (e)  $d$ - $q$  axis current commands at case 2; (f) Speed command and response at case 2.

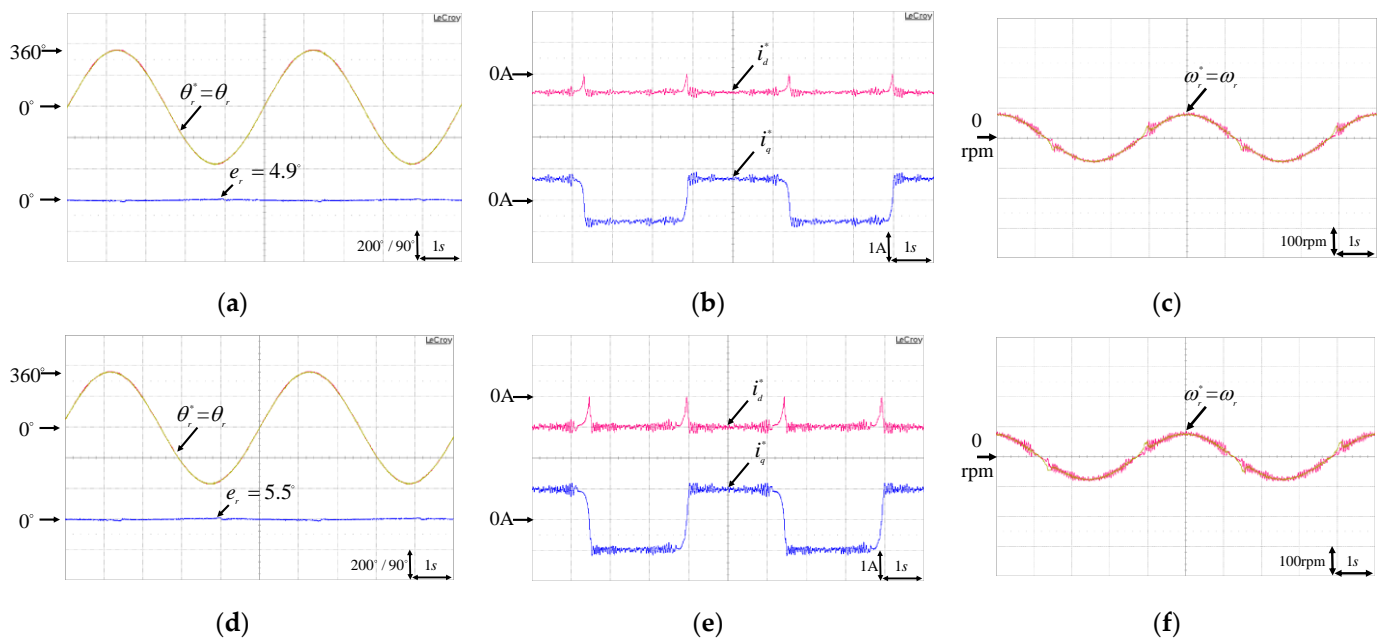


**Figure 15.** Experimental results of IBSCRWFNN control with periodical sinusoid command. (a) Position command, response, and error at case 1; (b)  $d$ - $q$  axis current commands at case 1; (c) Speed command and response at case 1; (d) Position command, response, and error at case 2; (e)  $d$ - $q$  axis current commands at case 2; (f) Speed command and response at case 2.

Figure 11 illustrates the experimental results of command tracking using periodical step commands for both case 1 and case 2 of the PI control system. The position command, response, and error are shown in Figure 11a,d; the current commands are shown in Figure 11b,e; the speed command and response are shown in Figure 11c,f. Figures 12 and 13 illustrate the experimental results of command tracking using periodical step and sinusoid commands for both case 1 and case 2 of the BSC control system. The position command, response, and error are shown in Figures 12a,d and 13a,d; the current commands are shown in Figures 12b,e and 13b,e; the speed command and response are shown in Figures 12c,f and 13c,f. In addition, Figures 14 and 15 illustrate the experimental results of command tracking using periodical step and sinusoid commands for both case 1 and case 2 of the IBSCRWFNN control system. The position command, response, and error are shown in Figures 14a,d and 15a,d; the current commands are shown in Figures 14b,e and 15b,e; the speed command and response are shown in Figures 14c,f and 15c,f.

From the experimental results, it can be observed that the  $d$ -axis current command is effectively generated using the FEA-based look-up table (LUT) for MTPA control. Moreover, the BSC position controller performs better than the PI controller, and the proposed IBSCRWFNN controller outperforms the BSC controller. The rotor response of the PMASynRM is significantly enhanced by the proposed IBSCRWFNN position controller, resulting in reduced tracking errors under different reference inputs. This improvement can be attributed to the parallel processing and online learning capabilities of the RWFNN used in the control network. In other words, the robustness of the position control is improved by employing the suggested IBSCRWFNN position controller. Furthermore, the quantified results of maximum tracking error and transient response time of all experiments are also presented in Table 3. In addition, the performance measurements of PI, BSC, and the proposed IBSCRWFNN position controllers are compared in Figure 16, considering two operating cases with periodical steps and sinusoid reference commands. The proposed IBSCRWFNN position controller exhibits lower maximum, average, and standard deviation tracking errors thanks to its faster convergence rate and improved generalization performance.

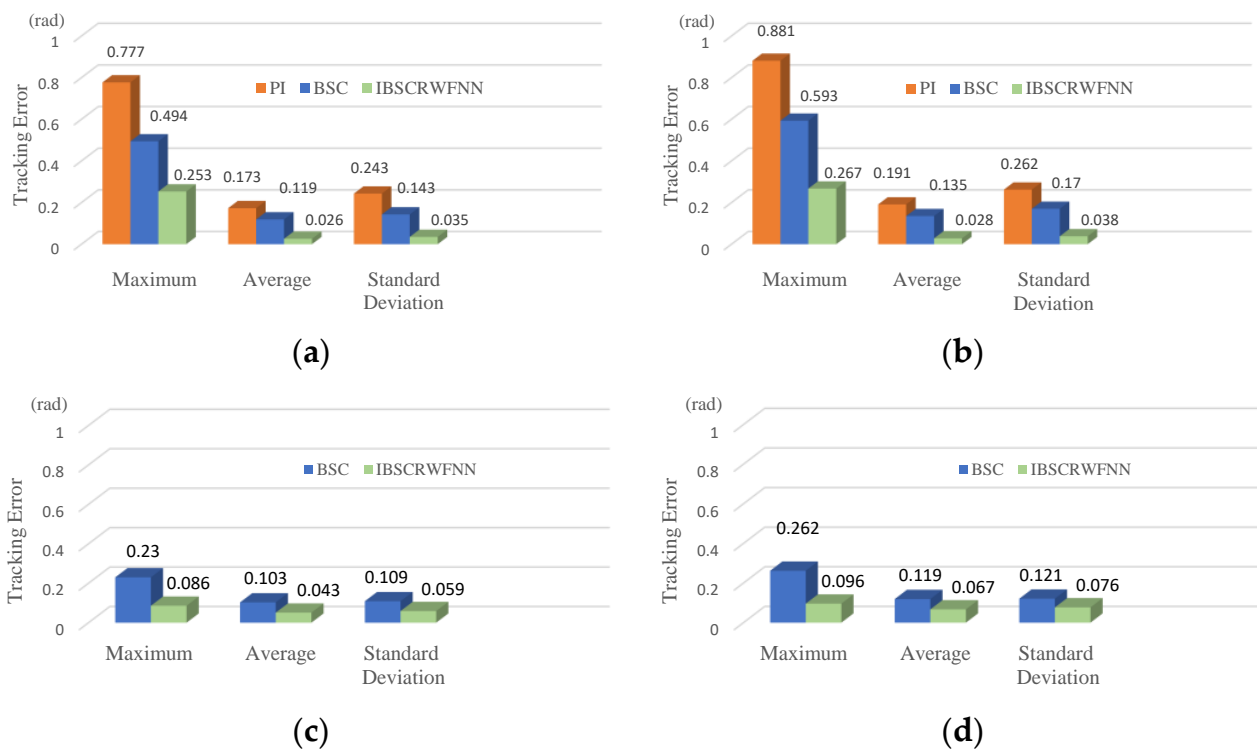


**Figure 16.** Maximum, average, and standard deviation of tracking errors used for the PI, BSC, and IBSCRWFNN. (a) Periodical step command at case 1; (b) Periodical step command at case 2; (c) Periodical sinusoid command at case 1; (d) Periodical sinusoid command at case 2.

## 7. Conclusions

In this study, an IBSCRWFNN control was proposed for a high-performance PMASynRM servo drive system. First, the dynamic model of the PMASynRM servo drive was analyzed using ANSYS Maxwell-2D capabilities. The FEA results were utilized to generate a LUT for the MTPA current angle command. Subsequently, a BSC position tracking system was developed to confront the existing lumped uncertainty of the motor drive. Moreover, the proposed RWFNN was employed as an alternative to the BSC law to address the challenges associated with the dynamic model of the motor required by the BSC in the PMASynRM servo drive. Furthermore, the Lyapunov stability method was employed to derive online learning algorithms for the RWFNN, ensuring asymptotical stability. Finally, the experimental results demonstrate that the proposed IBSCRWFNN exhibits excellent control performance in terms of position tracking control for the PMASynRM servo drive. This study presents several significant contributions, which include: (1) the successful creation of the IBSCRWFNN specifically designed for a high-performance PMASynRM position servo drive system; (2) the successful development of an online learning algorithm that allows for the real-time training of the RWFNN using the Lyapunov stability theorem; (3) the effective implementation of the IBSCRWFNN in a floating point DSP, ensuring robust position control performance for the high-performance PMASynRM.

The future works of this study are as follows: (1) in the experiment, an optical encoder was used to obtain the position of the motor rotor. Subsequently, a sensorless control method, which eliminates the need for sensors, can be further incorporated to reduce system costs. (2) In this study, the online learning rates of the intelligent control algorithm are adjusted through trial and error. In the future, it is possible to explore a self-adjusting network learning rate to optimize the intelligent control algorithm. (3) In addition to reducing motor copper losses by maximizing torque per ampere, the development of optimal efficiency control is also possible.

**Author Contributions:** F.-J.L. designed and developed the main parts of research work, including theory derivation and analyses of the obtained results. M.-S.H. were mainly responsible for the preparation of the paper. Y.-C.C. and S.-G.C. contributed to the DSP-based control platform and writing parts. All authors have read and agreed to the published version of the manuscript.

**Funding:** This research was funded by the National Science and Technology Council of Taiwan under Grant Most 110-2221-E-008-054-MY3.

**Institutional Review Board Statement:** Not applicable.

**Informed Consent Statement:** Not applicable.

**Data Availability Statement:** Data sharing is not applicable to this article.

**Conflicts of Interest:** The authors declare no conflict of interest.

## References

1. Lara, J.; Xu, J.; Chandra, A. Effects of Rotor Position Error in the Performance of Field Oriented Controlled PMSM Drives for Electric Vehicle Traction Applications. *IEEE Trans. Ind. Electron.* **2016**, *63*, 4738–4751. [\[CrossRef\]](#)
2. Yang, Y.; Sandra, M.C.; Rong, Y.; Berker, B.; Anand, S.; Hossein, D.; Ali, E. Design and Comparison of Interior Permanent Magnet Motor Topologies for Traction Applications. *IEEE Trans. Transp. Electr.* **2017**, *3*, 86–97. [\[CrossRef\]](#)
3. Fang, S.; Liu, H.; Wang, H.; Yang, H.; Lin, H. High Power Density PMSM with Lightweight Structure and High-Performance Soft Magnetic Alloy Core. *IEEE Trans. Appl. Supercond.* **2019**, *29*, 0602805. [\[CrossRef\]](#)
4. Kong, Y.; Lin, M.; Jia, L. A Novel High Power Density Permanent-Magnet Synchronous Machine with Wide Speed Range. *IEEE Trans. Magn.* **2020**, *56*, 7505206. [\[CrossRef\]](#)
5. Park, S.-H.; Lee, E.-C.; Park, J.-C.; Hwang, S.-W.; Lim, M.-S. Prediction of Mechanical Loss for High-Power-Density PMSM Considering Eddy Current Loss of PMs and Conductors. *IEEE Trans. Magn.* **2021**, *57*, 6300205. [\[CrossRef\]](#)
6. Bedetti, N.; Calligaro, S.; Petrella, R. Stand-Still Self-Identification of Flux Characteristics for Synchronous Reluctance Machines Using Novel Saturation Approximating Function and Multiple Linear Regression. *IEEE Trans. Ind. Appl.* **2016**, *52*, 3083–3092. [\[CrossRef\]](#)
7. Nikmaram, B.; Davari, S.A.; Naderi, P.; Garcia, C.; Rodriguez, J. Sensorless Simplified Finite Control Set Model Predictive Control of SynRM Using Finite Position Set Algorithm. *IEEE Access* **2021**, *9*, 47184–47193. [\[CrossRef\]](#)
8. Taghavi, S.M.; Pillay, P. A Mechanically Robust Rotor with Transverse Laminations for a Wide-Speed-Range Synchronous Reluctance Traction Motor. *IEEE Trans. Ind. Appl.* **2015**, *51*, 4404–4414. [\[CrossRef\]](#)
9. Ferrari, M.; Bianchi, N.; Doria, A.; Fornasiero, E. Design of synchronous reluctance motor for hybrid electric vehicles. *IEEE Trans. Ind. Appl.* **2015**, *51*, 3030–3040. [\[CrossRef\]](#)
10. Kerdsup, B.; Takorabet, N.; Nahidmobarakeh, B. Design of Permanent Magnet-Assisted Synchronous Reluctance Motors with Maximum Efficiency-Power Factor and Torque per Cost. In Proceedings of the 2018 XIII International Conference on Electrical Machines (ICEM), Alexandroupoli, Greece, 3–6 September 2018; pp. 2465–2471.
11. Wu, W.; Zhu, X.; Quan, L.; Du, Y.; Xiang, Z.; Zhu, X. Design and Analysis of a Hybrid Permanent Magnet Assisted Synchronous Reluctance Motor Considering Magnetic Saliency and PM Usage. *IEEE Trans. Appl. Supercond.* **2018**, *28*, 5200306. [\[CrossRef\]](#)
12. Nasiri-Zarandi, R.; Karami-Shahnani, A.; Toulabi, M.S.; Tassarolo, A. Design and Experimental Performance Assessment of an Outer Rotor PM-Assisted SynRM for the Electric Bike Propulsion. *IEEE Trans. Transp. Electr.* **2023**, *9*, 727–736. [\[CrossRef\]](#)
13. Liu, Z.; Hu, Y.; Wu, J.; Zhang, B.; Feng, G. A Novel Modular Permanent Magnet-Assisted Synchronous Reluctance Motor. *IEEE Access* **2021**, *9*, 19947–19959. [\[CrossRef\]](#)
14. Li, K.; Wang, Y. Maximum Torque Per Ampere (MTPA) Control for IPMSM Drives Based on a Variable-Equivalent-Parameter MTPA Control Law. *IEEE Trans. Power Electron.* **2019**, *34*, 7092–7102. [\[CrossRef\]](#)
15. Lin, F.J.; Liu, Y.T.; Yu, W.A. Power Perturbation Based MTPA with an Online Tuning Speed Controller for an IPMSM Drive System. *IEEE Trans. Ind. Electron.* **2018**, *65*, 3677–3687. [\[CrossRef\]](#)
16. Li, K.; Wang, Y. Maximum Torque per Ampere (MTPA) Control for IPMSM Drives Using Signal Injection and an MTPA Control Law. *IEEE Trans. Ind. Inform.* **2019**, *15*, 5588–5598. [\[CrossRef\]](#)
17. Yousefi-Talouki, A.; Pescetto, P.; Pellegrino, G. Sensorless Direct Flux Vector Control of Synchronous Reluctance Motors Including Standstill, MTPA, and Flux Weakening. *IEEE Trans. Ind. Appl.* **2017**, *53*, 3598–3608. [\[CrossRef\]](#)
18. Dianov, A.; Tinazzi, F.; Calligaro, S.; Bolognani, S. Review and Classification of MTPA Control Algorithms for Synchronous Motors. *IEEE Trans. Power Electron.* **2022**, *37*, 3990–4007. [\[CrossRef\]](#)
19. Kim, H.S.; Lee, Y.; Sul, S.K.; Yu, J.; Oh, J. Online MTPA Control of IPMSM Based on Robust Numerical Optimization Technique. *IEEE Trans. Ind. Appl.* **2019**, *55*, 3736–3746. [\[CrossRef\]](#)
20. Lin, F.J.; Huang, M.S.; Hung, C.Y.; Chien, Y.C. Intelligent Computed Torque Control with Recurrent Legendre Fuzzy Neural Network for Permanent-Magnet Assisted Synchronous Reluctance Motor. *IEEE Access* **2023**, *11*, 54017–54028. [\[CrossRef\]](#)
21. Liu, T.-H.; Pu, H.-T.; Lin, C.-K. Implementation of an Adaptive Position Control System of a Permanent-Magnet Synchronous Motor and Its Application. *IET Electr. Power Appl.* **2010**, *4*, 121–130. [\[CrossRef\]](#)

22. Lin, F.J.; Chen, S.G.; Hsu, C.W. Intelligent backstepping control using recurrent feature selection fuzzy neural network for synchronous reluctance motor position servo drive system. *IEEE Trans. Fuzzy Syst.* **2019**, *27*, 413–427. [[CrossRef](#)]
23. Mansouri, M.M.; Hadjeri, S.; Brahami, M. New method of detection, identification, and elimination of photovoltaic system faults in real time based on the adaptive Neuro-fuzzy system. *IEEE J. Photovolt.* **2021**, *11*, 797–805. [[CrossRef](#)]
24. Dong, C.; Yu, Z.; Chen, X.; Chen, H.; Huang, Y.; Huang, Q. Adaptability Control Towards Complex Ground Based on Fuzzy Logic for Humanoid Robots. *IEEE Trans. Fuzzy Syst.* **2022**, *30*, 1574–1584. [[CrossRef](#)]
25. Chen, S.Y.; Liu, T.S. Intelligent tracking control of a PMLSM using self-evolving probabilistic fuzzy neural network. *IET Electr. Power Appl.* **2017**, *11*, 1043–1054. [[CrossRef](#)]
26. Lin, F.J.; Sun, I.F.; Yang, K.J.; Chang, J.K. Recurrent Fuzzy Neural Cerebellar Model Articulation Network Fault-Tolerant Control of Six-Phase Permanent Magnet Synchronous Motor Position Servo Drive. *IEEE Trans. Fuzzy Syst.* **2016**, *24*, 153–167. [[CrossRef](#)]
27. Fei, J.; Chen, Y.; Liu, L.; Fang, Y. Fuzzy Multiple Hidden Layer Recurrent Neural Control of Nonlinear System Using Terminal Sliding-Mode Controller. *IEEE Trans. Cybern.* **2022**, *52*, 9519–9534. [[CrossRef](#)] [[PubMed](#)]
28. Khan, M.A.; Uddin, M.N.; Rahman, M.A. A Novel Wavelet-Neural-Network-Based Robust Controller for IPM Motor Drives. *IEEE Trans. Ind. Appl.* **2013**, *49*, 2341–2351. [[CrossRef](#)]
29. Huang, W.; Oh, S.; Pedrycz, W. Fuzzy Wavelet Polynomial Neural Networks: Analysis and Design. *IEEE Trans. Fuzzy Syst.* **2017**, *25*, 1329–1341. [[CrossRef](#)]
30. Lin, F.J.; Tan, K.H.; Luo, W.C.; Xiao, G.D. Improved LVRT performance of PV power plant using recurrent wavelet fuzzy neural network control for weak grid conditions. *IEEE Access* **2020**, *8*, 69346–69358. [[CrossRef](#)]

**Disclaimer/Publisher’s Note:** The statements, opinions and data contained in all publications are solely those of the individual author(s) and contributor(s) and not of MDPI and/or the editor(s). MDPI and/or the editor(s) disclaim responsibility for any injury to people or property resulting from any ideas, methods, instructions or products referred to in the content.